Journal of Environmental Chemical Engineering 10 (2022) 108665

Contents lists available at ScienceDirect

Journal of Environmental Chemical Engineering

journal homepage: www.elsevier.com/locate/jece

Efficient chromium (VI) removal from wastewater by adsorption-assisted photocatalysis using MXene

Nur Shafiqah Jamaluddin [a], Nur Hashimah Alias [a,*], Sadaki Samitsu [b], Nur Hidayati Othman [a], Juhana Jaafar [c], Fauziah Marpani [a], Woei Jye Lau [c], Yong Zen Tan [d]

[a] Department of Oil and Gas Engineering, School of Chemical Engineering, College of Engineering, Universiti Teknologi MARA, 40450 Shah Alam, Selangor, Malaysia
[b] Research and Services Division of Materials Data and Integrated System (MaDIS), National Institute for Materials Science (NIMS), 1–2-1 Sengen, Tsukuba, Ibaraki 305–0047, Japan
[c] Advanced Membrane Technology Research Centre (AMTEC), School of Chemical and Energy Engineering, Faculty of Engineering, Universiti Teknologi Malaysia, 81310 Skudai, Johor, Malaysia
[d] School of Chemistry, Chemical and Biotechnology Engineering, Nanyang Technological University, Singapore 637459, Singapore

ARTICLE INFO

Editor: Ana Loncaric Bozic

Keywords:
MXene
Chromium (VI)
Adsorption
Photocatalysis
Wastewater

ABSTRACT

Hexavalent chromium, Cr(VI), is considered hazardous heavy metal in water bodies that can cause severe effects on human health and the environment. Over the years, myriad attention has been focused on developing photocatalysts to remove Cr(VI) from wastewater. However, broad bandgap energy and the high electron recombination rate of these conventional photocatalysts have limited their photocatalytic ability. Therefore, efficient photocatalytic materials for Cr(VI) removal in wastewater is strongly demanded. In this study, delaminated MXene was successfully synthesised and used to remove Cr(IV) from the aqueous solution. The synthesised delaminated MXene was characterised using XRD, EDX, FTIR, FESEM, nitrogen adsorption-desorption analysis, TGA, UV-Vis-NIR spectroscopy and XPS. Based on the results, the optimum operating conditions for Cr(VI) removal by the synthesised MXene was obtained at pH 4 with photocatalyst loading of 1.5 g/L and Cr(VI) initial concentration of 5 mg/L. The removal efficiency of Cr(VI) via adsorption-assisted photocatalysis over various concentrations was around 3.1–28.9% higher than adsorption, verifying a synergistic effect of adsorption and photocatalysis by the delaminated MXene. The isotherm of Cr(VI) adsorption was fitted by the Langmuir model ($R^2 > 0.9848$) and was found better than the Freundlich model ($R^2 > 0.8824$). Meanwhile, the time dependence of Cr(VI) adsorption was well fitted to the pseudo-second-order kinetic model with $R^2 > 0.9999$. In conclusion, the results obtained suggest that the delaminated MXene possesses excellent properties and the ability to remove Cr(VI) via adsorption-assisted photocatalysis and has great potential to be used for industrial wastewater applications.

1. Introduction

In recent years, significant improvement in water purification technology has been strongly demanded because a large volume of wastewater containing heavy metals is discharged in many industrial processes such as electroplating, metal coating, electropolishing, inferior cosmetic raw materials, and leather tanning [1,2]. Chromium is one of the most prevalent heavy metals in industrial wastewater, which mainly exists as Cr(VI) and Cr(III) [3]. Cr(III) is relatively less harmful as it has low mobility in water and soil. It is also an essential micronutrient to maintain the metabolism of proteins, lipids, and sugars in the human body [1,4]. Oppositely, Cr(VI) is highly toxic, leading to serious health issues such as kidney failure, skin sensitivity, lung cancer, genetic defects, liver damage, and even death [4–6]. Therefore, according to the World Health Organization (WHO) recommendation, the maximum tolerable concentration of Cr(VI) in drinking water should not exceed 0.05 mg/L [5]. In this regard, separation and purification technology are necessary for the chemical engineering field to eliminate Cr(VI) and convert it to less toxic trivalent chromium, Cr(III), from effluent wastewater. Various approaches have been examined to remove Cr(VI) including ion exchange [7,8], chemical precipitation [9], membrane process [10,11], electrochemical treatment [12], adsorption [11,13],

* Corresponding author.
E-mail address: nurhashimah@uitm.edu.my (N.H. Alias).

https://doi.org/10.1016/j.jece.2022.108665
Received 8 March 2022; Received in revised form 28 August 2022; Accepted 27 September 2022
Available online 30 September 2022
2213-3437/© 2022 Elsevier Ltd. All rights reserved.

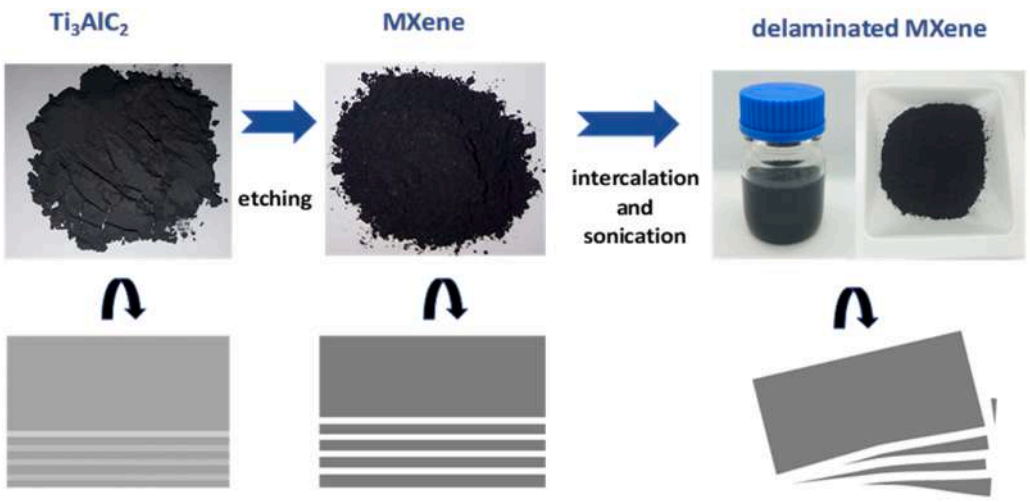

Scheme 1. Schematic illustration of the delaminated MXene synthesis procedure.

and photocatalysis [14–17]. Photocatalysis assisted by nanomaterials is a promising method for the purification process of ion-contaminated wastewater. The nanomaterials effectively capture water-soluble harmful ions via physical and chemical adsorption and can transform the ions into another less harmful ion species by photo-assisted chemical reaction. The process is as favourable as separation and purification methods due to high removal efficiency, environmental friendliness, and low energy cost [15]. Thus, green technology of photocatalysis, which uses solar energy or a source of light irradiation, has gained attraction among many researchers as it consists of photocatalytic reduction and photocatalytic oxidation for various pollutants in wastewater, including metal ions [18], dyes [19,20], polychlorinated biphenyls and phenols [21]. A recent study demonstrated that Zn-Al-layered double hydroxide and TiO_2 composites have higher Cr(VI) removal efficiency than simple adsorption [22]. According to this study, several photocatalytic adsorbents have been examined for Cr(VI) removal from wastewater: metal sulphide [23,24], zinc oxide [17,25], and titanium dioxide [16,26]. However, they possess some limitations and poor photocatalysis performance due to the broad bandgap energy and high electron recombination rate of the photocatalysts. Therefore, an efficient photocatalytic adsorbent effective for Cr(VI) removal in wastewater is strongly demanded [27].

In 2011, a new member of two-dimensional (2D) nanomaterial, called MXene, was discovered by Naquib et al., from Drexel University [28], comprising transition metal carbides, carbonitrides, and nitrides [29] is one of the attractive photocatalyst material used for many pollutants removal due to its porous structure, water affinity, superior electrical conductivity, excellent structural stabilities, tunable interlayer spacing [30,31], sufficient bandgaps energy [32–35]. MXene is denoted by a general formula of $M_{n+1}X_nT_x$ where M represents the transition metals, X represents either carbon or nitrogen, n represents any number (n = 1, 2, 3, etc.), and T_x is surface functional groups (–O, –OH, –Cl, or –F) [36–39]. Numerous published papers have highlighted the success of MXene in photocatalysis, especially in N_2 fixation, CO_2 reduction, water splitting and pollutant degradation [40]. Moreover, MXene also has been widely applied as an auxiliary photocatalyst because it has a narrow band gap and excellent light absorption that can help other photoactive materials harvest light. For instance, Zhang and co-workers [41] had prepared TiO_2 to crystallise and in situ growth between MXene layers for efficient adsorption and photocatalysis.

MXene was also provenly efficient for the degradation of dyes and removal of heavy metal ions such as Cu(II) [42], Pb(II) [43], Hg(II) [44,45], and Cr(VI) [46–48]. Mashtalir et al., [49] reported that MXene could be used as a photocatalyst to enhance the photodegradation of M. B. and AB80 dyes. Furthermore, MXene behaves as a photocatalyst for arsenic (As) species and 94% removal of As species was demonstrated under ultraviolet (UV) light irradiation [18]. Recently, a few-layer MXene sheets structure, called delaminated MXene, was synthesised by intercalating $Ti_3C_2T_x$ surface with a suitable solvent followed by bath sonication [50]. The reported adsorption capacity of delaminated MXene for Pb(II) removal was 2.7 times higher than commercial activated carbon [50]. However, up to the recent, no work has been reported in detail on the removal of Cr(VI) using delaminated MXene via photocatalysis process.

Therefore, this study inspires to demonstrate the adsorption-assisted photocatalytic ability of delaminated MXene that is effective on Cr(VI) removal in an aqueous solution for the first time. Delaminated MXene was prepared by etching the aluminium (Al) constituent from ternary layered carbide (Ti_3AlC_2) and was characterised by its physicochemical and thermal properties. Cr(VI) removal performance was evaluated by varying pHs, photocatalyst loadings, and Cr(VI) solution concentration. A possible Cr(VI) removal mechanism via adsorption-assisted photocatalysis was also proposed based on the adsorption isotherm, kinetic study and characterisation results of the synthesised delaminated MXene.

2. Materials and methods

2.1. Materials

Layered ternary carbide (Ti_3AlC_2, MAX) powders (>99 wt% purity) was supplied by Nanoshel (Intelligent Materials Pvt Ltd). Hydrofluoric acid (HF, 49%) and dimethyl sulfoxide (DMSO, 99%) were purchased from Sigma Aldrich Co., Inc. All chemicals were used without further purification. Deionised water was used for washing and experimental works.

2.2. Preparation of Cr(VI) stock solution

Potassium dichromate ($K_2Cr_2O_7$) was used as the source to prepare the stock solution of chromium. A 1000 mg/L of Cr(VI) stock solution was freshly prepared by dissolving 2.75 g of $K_2Cr_2O_7$ (99% purity) into 1000 mL of deionised water in a 1 L volumetric flask.

2.3. Preparation of delaminated MXene ($Ti_3C_2T_x$)

The preparation of delaminated MXene consists of the etching and delamination process by a method previously reported by [25,44], as schematically illustrated in Scheme 1. In the etching process, 1.0 g graphitic-greyish Ti_3AlC_2 consisting of layered MAX phase was

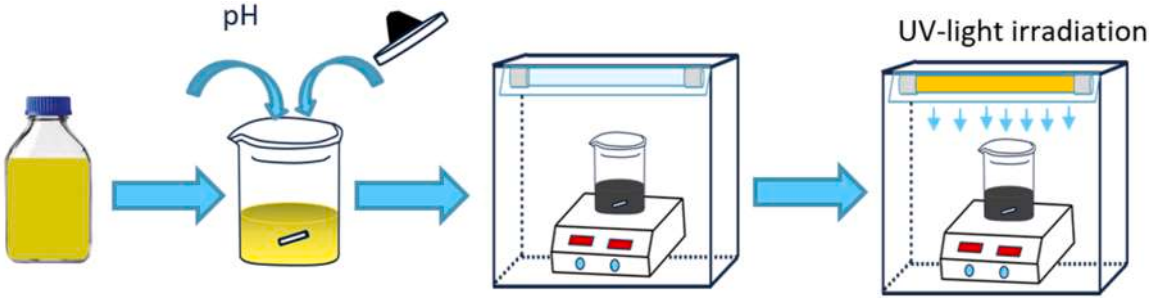

Scheme 2. Schematic illustration of Cr(VI) removal via photocatalysis under UV light irradiation.

gradually immersed in 28 mL of 10 wt% aqueous hydrofluoric acid (HF) in a 60 mL polypropylene (PP) bottle for 24 h under vigorous magnetic stirring. Sedimented solids were collected via centrifugation at 5000 rpm for 5 min and washed with deionised water to completely remove contaminants until the pH of the dispersion was stabilised around pH 6. The solids were dried in an oven at 70 °Cfor 24 h, and a few layers of MXene ($Ti_3C_2T_x$) were collected as black solids. In the subsequent delamination process, the MXene was immersed in 12 mL of dimethyl sulfoxide (DMSO) for 20 h at room temperature, followed by bath sonication for 30 min. After that, the delaminated $Ti_3C_2T_x$ was washed with deionised water and collected by centrifugation at 10000 rpm for 1 h. Finally, it was dried at 120 °C fo Overall, approximately 80% yield of delaminated MXene was obtained from Ti_3AlC_2.

2.4. Characterisation

The crystalline structure of Ti_3AlC_2 and delaminated MXene were analysed using X-ray diffraction (XRD, D/Max 2550 PC, Rigaku, Japan) using Cu Kα radiation ($\lambda = 0.154$ nm) with an accelerating voltage of 40 kV and current of 30 mA. The diffraction patterns were recorded over the diffraction angle 2θ between 2° and 80° at a scan rate of 5°/min. XRD result was also used to estimate the grain size of delaminated MXene using the Scherrer formula: $D = k\lambda/\beta \cos \theta$, where $k = 0.9$, $\lambda = 0.154$ nm, $\beta =$ the broadening peak width at the half peak height in radians, and $\theta =$ Bragg angle [51]. The morphology of Ti_3AlC_2 and delaminated MXene was observed using a Field emission scanning electron microscope (FESEM, S-4800, Hitachi High Tech. Co.). The elemental mappings of Ti_3AlC_2 and delaminated MXene were quantified using an energy dispersive X-ray analyser (EDX., Oxford Instruments U. S.A.) attached to FESEM. Nitrogen adsorption/desorption measurement was performed using the Micromeritics ASAP 2020 system at − 196 °C. Prior to the measurement, samples were dried at 120 °C for 5 h. The specific surface area of the prepared samples was measured using Brunauer–Emmett–Teller (BET) analysis. The thermal stability of the prepared delaminated MXene was evaluated using a thermogravimetric analyser (TGA4000, Perkin Elmer Inc.) under nitrogen gas at a heating rate of 10 °C/min to 800 °C. Fourier transform infrared spectroscopy (FTIR, Perkin-Elmer, USA) with transmission configuration was employed to analyse the chemical structure of delaminated MXene before and after Cr(VI) adsorption. The prepared samples were ground with potassium bromide (KBr) at a weight ratio of 1:10 and pressed into pellets to reduce undesirable scattering by air void. Under ambient conditions, FTIR spectra were recorded at the wavenumber range of 500–4000 cm^{-1}. The optical band gap of the synthesised delaminated MXene was analysed by a 750 UV-Vis spectrometer PerkinElmer along with 60-mm integrating sphere. The band gap energy of the delaminated MXene was estimated using the Kubelka–Munch function by plotting $(\alpha h\nu)^2$ versus $h\nu$ [52], where α is the absorption coefficient, and hv is the photon energy. It was obtained by determining a straight graph segment from the Tauc plot technique [53]. X-ray photoelectron spectroscopy (XPS) measurements were carried out using XPS Quantera II (ULVAC PHI) with an X-ray source of Al Kα (1486 eV).

2.5. Adsorption and photocatalysis measurements

A freshly prepared Cr(VI) stock solution was diluted to a targeted concentration prior to the adsorption and photocatalysis experiment. The Cr(VI) solution was set at a pH range of 2–6 using 0.1 M HCl and 0.1 M NaOH. Adsorption measurement of Cr(VI) was conducted under dark conditions for 3 h. Meanwhile, for the photocatalysis measurement, Cr(VI) solution was suspended well with a photocatalyst under dark conditions for 30 min. After that, the suspension solution was irradiated under UV light for 3 h. Scheme 2 illustrates Cr(VI) removal via photocatalysis under UV light irradiation. The change of Cr(VI) concentration was measured using Cary 60 ultraviolet-visible (UV-Vis) spectrophotometer via the 1,5-dipenylcarbazide method at a wavelength of 543 nm [54]. In addition, atomic absorption spectroscopy (AAS, Z-2000, Hitachi) was used to quantify the amount of Cr(VI) reduction to Cr(III) in the solution after the reaction. Before AAS and UV-Vis measurement, the sample solution was filtered using a polyethersulfone (PES) syringe filter (0.22 μm). The adsorption capacity (mg/g) and removal percentage (%) were calculated using Eq. 1 and Eq. 2.

$$\text{Adsorption capacity,} \quad (\text{mg}/\text{g}) = \frac{c_i - c_e}{\text{m}} V \tag{1}$$

$$\text{Removal percentage}(\%) = \left(\frac{c_i - c_e}{c_i}\right) \times 100 \tag{2}$$

Where c_i is the initial Cr(VI) concentration (mg/L), c_e is the final Cr(VI) concentration (mg/L) at their respective times (min), m is the mass of the delaminated MXene (g), and V is the volume of the solution (L).

Meanwhile, the adsorption isotherm of Cr(VI) was fitted using Langmuir, Freundlich, Temkin and Dubinin–Radushkevich (D-R) isotherm models [55,56]. The linearised forms of the model equations are expressed in Eqs 3–6.

Langmuir model

$$\frac{c_e}{q_e} = \frac{1}{K_L q_{max}} + \frac{c_e}{q_{max}} \tag{3}$$

Freundlich model

$$\log q_e = \log K_F + \frac{1}{n} \log c_e \tag{4}$$

Temkin model

$$q_e = B \ln_A + B \ln C_e \tag{5}$$

Dubinin–Radushkevich (D-R) isotherm model

$$\ln q_e = \ln Q_D - K\varepsilon^2 \tag{6}$$

Where c_e is the final concentration of Cr(VI) in mg/L at respective times. q_e (mg/g) is the adsorption capacity of Cr(VI) at equilibrium, q_{max} (mg/g) is the maximum capacity amount of Cr(VI) per unit weight of delaminated MXene, K_L(L/mg) is the Langmuir isotherm constant, and K_F(mg/g)(L/mg)(1/n) and n are the Freundlich isotherm constants. B

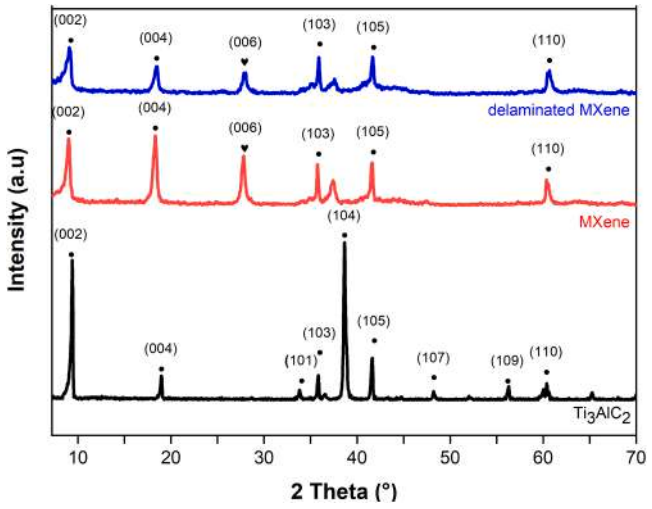

Fig. 1. XRD patterns of Ti_3AlC_2, MXene, and delaminated MXene.

(J/mol) represent a constant for heat adsorption, and A (L/mg) is the equilibrium binding constant that correlates to the maximum binding energy for the Temkin model. In Dubinin-Radushkevich (D-R) model, Q_D (mg/g) represent the maximum D-R adsorption capacity, whereas $\mathcal{E}$ (KJ/mol) is the polyani potential energy. The kinetic study of Cr(VI) adsorption was evaluated at the optimal loading of delaminated MXene and Cr(VI) concentration within 7 h. At every 1 h interval, 4 mL of Cr (VI) solution sample was collected and measured using AAS. The time dependence of the Cr(VI) adsorption experiment was fitted using pseudo-first and pseudo-second-order kinetic models [45–47] and intraparticle diffusion and liquid film diffusion models [56]. The linear forms of kinetic models are expressed in Eqs 7–10.

Pseudo-first order

$$\ln(q_e - q_t) \quad = \ln q_e - k_1 t \tag{7}$$

Pseudo-second order

$$\frac{t}{q_t} = \frac{1}{k_2 q_e^{\,2}} + \frac{1}{q_e} \tag{8}$$

Intra-particle diffusion

$$q_t = k_1 t + \mathrm{C} \tag{9}$$

Liquid film diffusion model

$$\ln\left(1 - \frac{q_t}{q_e}\right) = k_{id}\mathrm{t} \tag{10}$$

where k_1, k_2 and k_{id} are the rate constants and q_t (mg/g), is the adsorption capacity at a specific time t.

3. Results and discussion

3.1. Characterisation of MXene

To evaluate the crystalline structure and interlayer spacing of the samples, XRD analysis was carried out on Ti_3AlC_2, MXene, and delaminated MXene (Fig. 1). Ti_3AlC_2 presents an intense peak at $2\theta = 39°$, corresponding to (104) in Ti_3AlC_2. After etching Ti_3AlC_2 by 10 wt % HF, MXene, and delaminated MXene lost the (104) peak completely, and a new peak appeared approximately at 27.8°, corresponding to (006) diffraction. An indistinct peak of TiC impurity was found at 37°. Moreover, the main diffraction peaks of Ti_3AlC_2 became weaker and broader after undergoing the etching and delamination processes. The results indicate that etching by 10 wt% HF successfully ruptured the Ti-Al metal bond and removed the Al element in Ti_3AlC_2 due to weak bond energy in Ti_3AlC_2 [32]. After the delamination process, all the XRD peaks remained, and the observable peak (002) was shifted from 9.4° to 8.9°, confirming an increase in interlayer layer spacing without the loss of significant peaks. Most of the peaks became broad, consistent with the decrease in crystallinity by delamination. A similar observation was reported by other researchers [57]. In addition, estimation of grain sizes using the Scherrer formula has found that the grain size of delaminated MXene (26.2 nm) decreased 28% and 18% as compared to Ti_3AlC_2

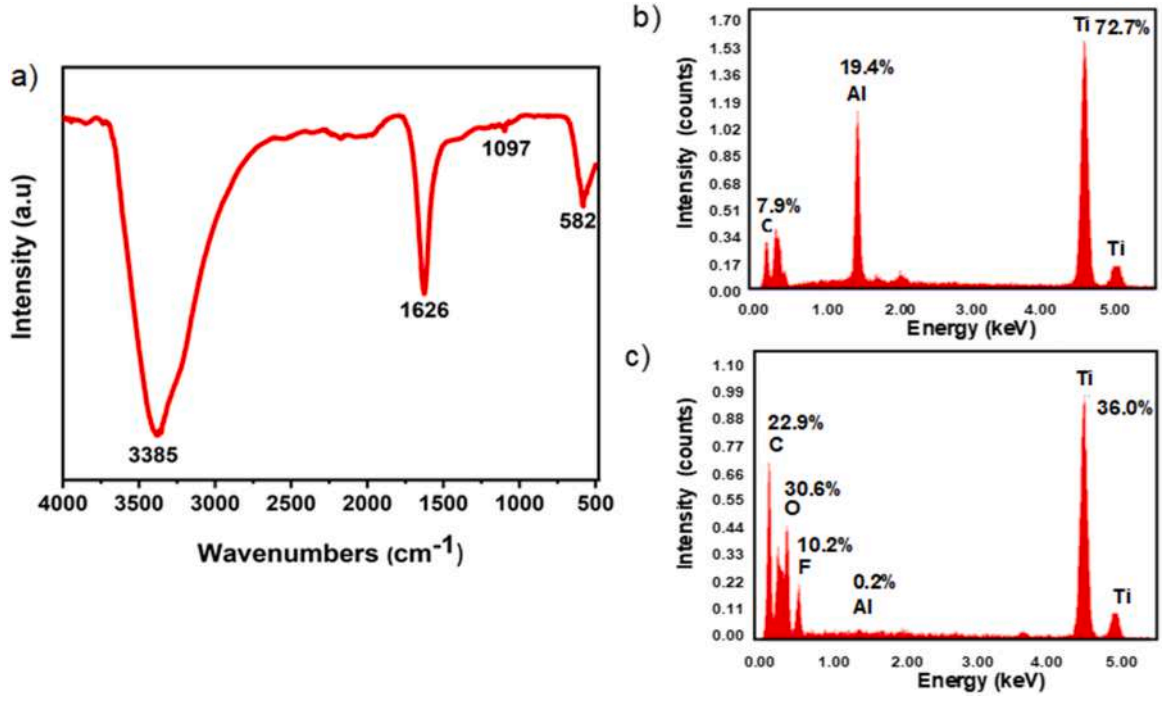

Fig. 2. a) FTIR spectra of delaminated MXene, b) EDX spectrum of Ti_3AlC_2, and c) EDX spectrum of delaminated MXene (All the peaks were normalised to the peak intensity of Ti).

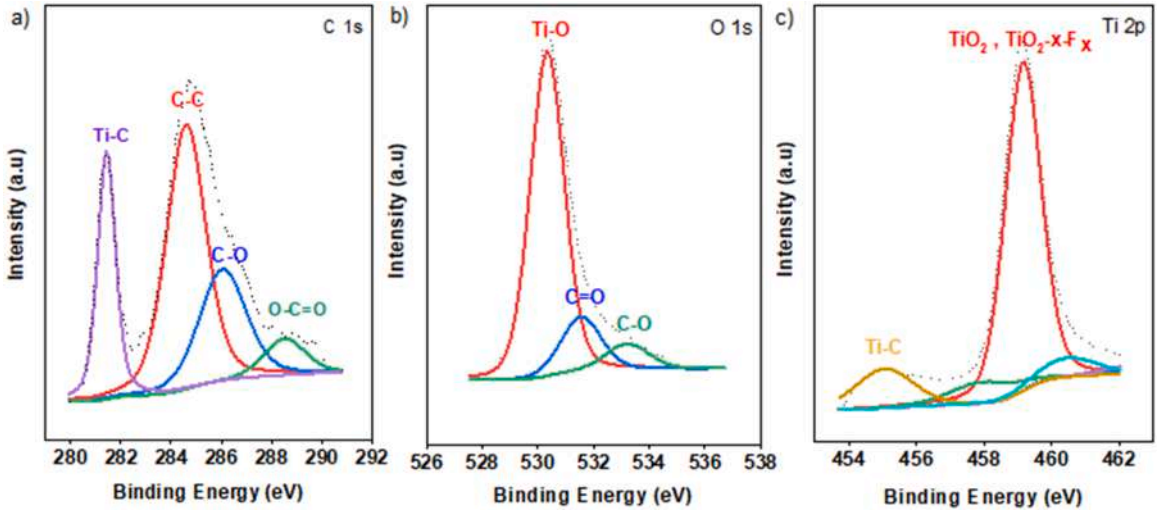

Fig. 3. XPS spectra of fresh delaminated MXene.

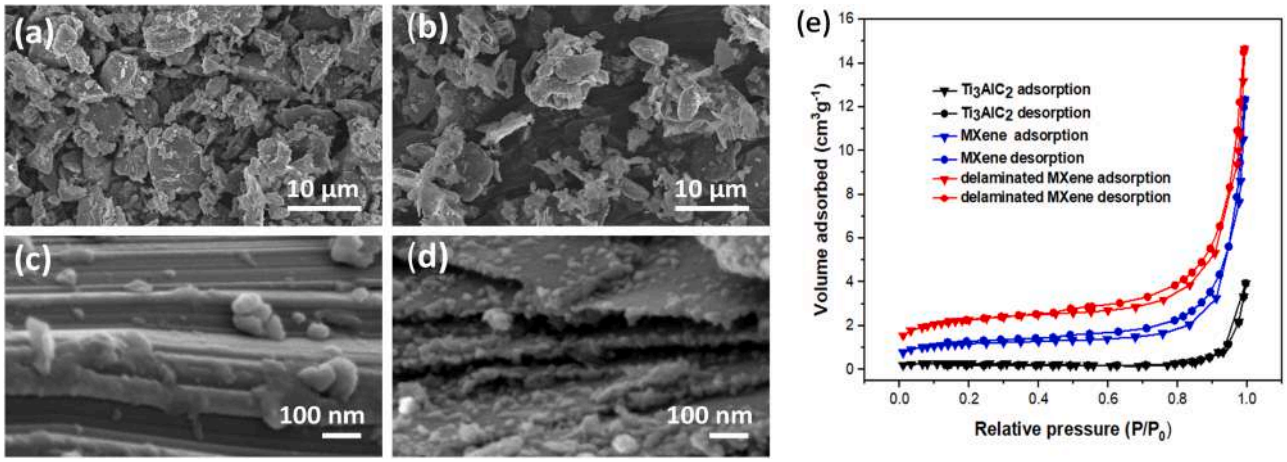

Fig. 4. Surface and cross-sectional FESEM images of (a and c) Ti_3AlC_2, (b and d) delaminated MXene and e) Nitrogen adsorption/desorption analysis of Ti_3AlC_2 and delaminated MXene.

(36.2 nm) and MXene (31.9 nm), respectively, thus confirmed that MXene has successfully delaminated through etching and delamination processes.

FTIR analysis was conducted to verify the functional groups of delaminated MXene. Based on Fig. 2(a), it was observed that the peak at 3381 cm^{-1} in the FTIR spectra was mainly attributed to the–OH stretching vibrations, whereas the distinctive peak at 1626 cm^{-1} is represented by H–OH stretching bands [58]. Likewise, the broadband at 3400 cm^{-1} is attributed to the –OH stretching vibrations of $Ti_3C_2T_x$. Meanwhile, the distinctive peak at 1636 cm^{-1} belongs to the H–OH stretching bands and confirms the existence of the–OH group and water moieties on the $Ti_3C_2T_x$ surface. In addition, the typical peak of 1097 cm^{-1} signifies the deformation vibrations of the C–F bond. Lastly, a stretching vibration peak at 582 cm^{-1} was observed due to the Ti-O-Ti bond [59]. These findings agree with other reported studies on MXene [60,61].

Fig. 2(b and c) show the EDX spectrum of the prepared samples, where the sharp peak of Al in Ti_3AlC_2 decreased tremendously after the delamination process. The calculated atomic percentage of Al reduced from 19.5 at% in Ti_3AlC_2 to 0.2 at% in the delaminated MXene. The negligible amount of Al indicates the effective etching process by HF. The synthesised delaminated MXene also displayed the peaks of titanium, Ti (36 at%), oxygen, O (30.6 at%), carbon, C (22.9 at%) and fluorine, F (10.2 at%). Ti and C are attributed to the elements of Ti_3AlC_2, whereas O and F probably are the result of the etching reaction by HF.

These findings were quantitatively confirmed by XPS analysis. Fig. 3 (a-c) displayed XPS spectra of C 1 s, O 1 s and Ti 2p in the synthesised fresh delaminated MXene. In the C 1 s spectrum, the assigning peak at 281.43 represents the Ti–C bond, whereas the other three peaks at 284.57, 286.01 and 288.53 represent C–C, C–O and O–C = O bonds, respectively. Meanwhile, the O 1 s spectrum revealed that the characteristic peaks observed at 530.34, 531.57 and 533.21 eV are assigned to the Ti-O, C═C and C-O bonds, respectively. Ti 2p spectra showed peaks at 455.09 and 459.18, indicating Ti–C and TiO_2 or TiO_2–x–Fx species. The observed functional groups detected in the FTIR and XPS spectrum agree with the elements presented in the EDX result. Furthermore, the findings agree with other reported studies on MXene [60,61]. These results prove that the delaminated MXene contained abundant –OH and small amounts of –F, –OH, and –COOH as terminal groups on the sheet structure in the delaminated MXene.

The EDX. result showed O was more dominant than F, possibly due to the low concentration of HF used in the etching process. The low concentration of HF was preferable to minimise the terminal groups of –F as the availability of –F can possess hydrophobic characteristics, which might reduce the ability of Ti_3C_2 sheets to intercalate with water. Particularly, 10 wt% concentration of HF was strong enough to allow

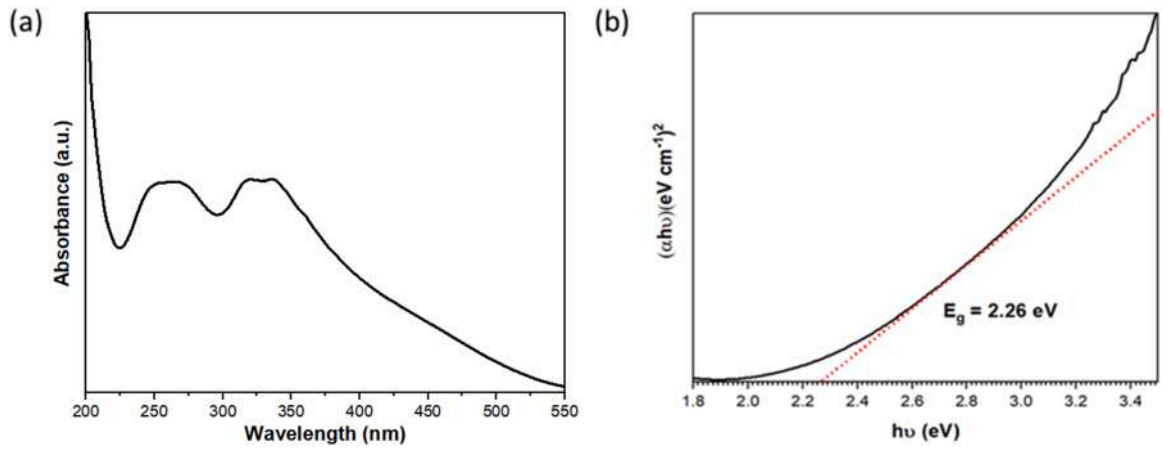

Fig. 5. a) UV-Vis-NIR absorption spectra and b) bandgap energy of delaminated MXene.

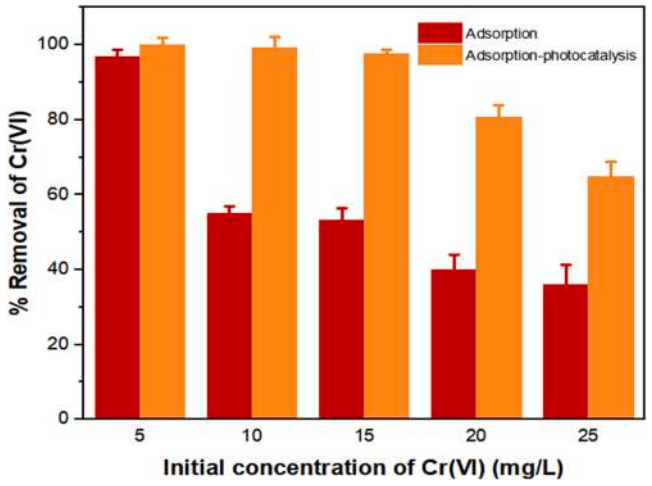

Fig. 6. Comparison on percentage (%) removal of Cr(VI) via adsorption and adsorption-assisted photocatalysis at different Cr(VI) concentrations.

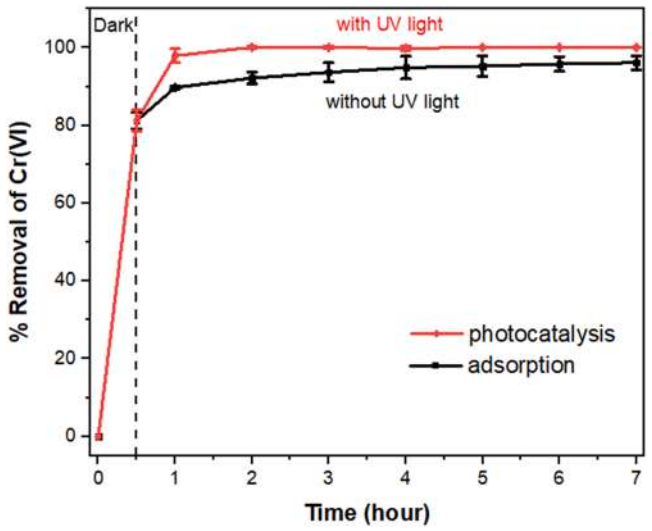

Fig. 7. Percentage (%) removal of Cr(IV) by adsorption and photocatalysis with photocatalyst loading of 1.5 g/L and Cr(VI) initial concentration of 5 mg/L pH).

the O:OH ratio as the main terminal group, indicating that Tx was mostly represented by –OH functional groups. These findings agree with previously published research work reported on MXene [60–63].

Fig. 4 shows the surface and cross-sectional FESEM images of $Ti_3AlC_2$and delaminated MXene. The top-view surface of Ti_3AlC_2 displays an irregular shape structure (Fig. 4a), and delaminated MXene has a crumpled shape with numerous ridges and rough surfaces (Fig. 4b) which presents the morphological difference of Ti_3AlC_2 after the etching and delamination processes. The layered structures of Ti_3AlC_2 and delaminated MXene were observed on the cross-sectional FESEM images shown in Fig. 4(c and d). In comparison to Fig. 4(c), Fig. 4(d) confirm the formation of delaminated MXene, yielding a morphology of a few-layer structure with less than 100 nm of interlayer spacing which concludes the successful removal of the Al layers from Ti_3AlC_2 after the etching and delamination process. Similar findings were also reported in previously reported studies [45,47].

Nanoporous structures of Ti_3AlC_2 and as-synthesised delaminated MXene were evaluated using nitrogen gas adsorption (Fig. 4e). MXene and delaminated MXene displayed a type IV isotherm which indicates the delaminated MXene is a mesoporous material, whereas Ti_3AlC_2 showed a type I isotherm corresponding to macroporous or non-porous morphology [47]. The specific surface area determined via BET analysis was 1.8 m^2/g for Ti_3AlC_2 and 4.2 m^2/g for MXene. The specific surface area of the synthesised delaminated MXene substantially increased after removing the Al layers using the etching process. Upon delamination, the synthesised delaminated MXene increased to 8.2 m^2/g due to an increase in pore volume. These results demonstrated the intercalation of DMSO and bath sonication contributed to enlarging the interlayer space of the synthesised delaminated MXene, facilitating accessible sites for adsorption [47,64]. Therefore, from adsorption and desorption analysis, delaminated MXene adsorbed the highest amount of N_2 compared to MXene and Ti_3AlC_2. The increment of the specific surface area is also beneficial in enhancing the photocatalytic activity of MXene.

The thermogravimetric analysis of the prepared delaminated MXene samples was carried out at a temperature range of 30–800 °C. Thermal degradation of delaminated MXene can be divided into three stages [46, 58,65]. In the first stage, 4–5% weight loss of delaminated MXene from room temperature to 200 °C originated from the adsorbed water molecules on the delaminated MXene surface [58]. Meanwhile, the weight loss in the second stage at a temperature above 200 °C was due to the degradation of delaminated MXene functional groups like –OH. On top of that, this was also influenced by the degradation of interlayer ions found on the surface of delaminated MXene. Finally, the final weight loss in the third stage is between the temperature of 470 and 700 ℃ due to the degradation of the layered arrangement of delaminated MXene with around 6–10% of weight loss. These findings demonstrated that delaminated MXene has high thermal properties in terms of thermal

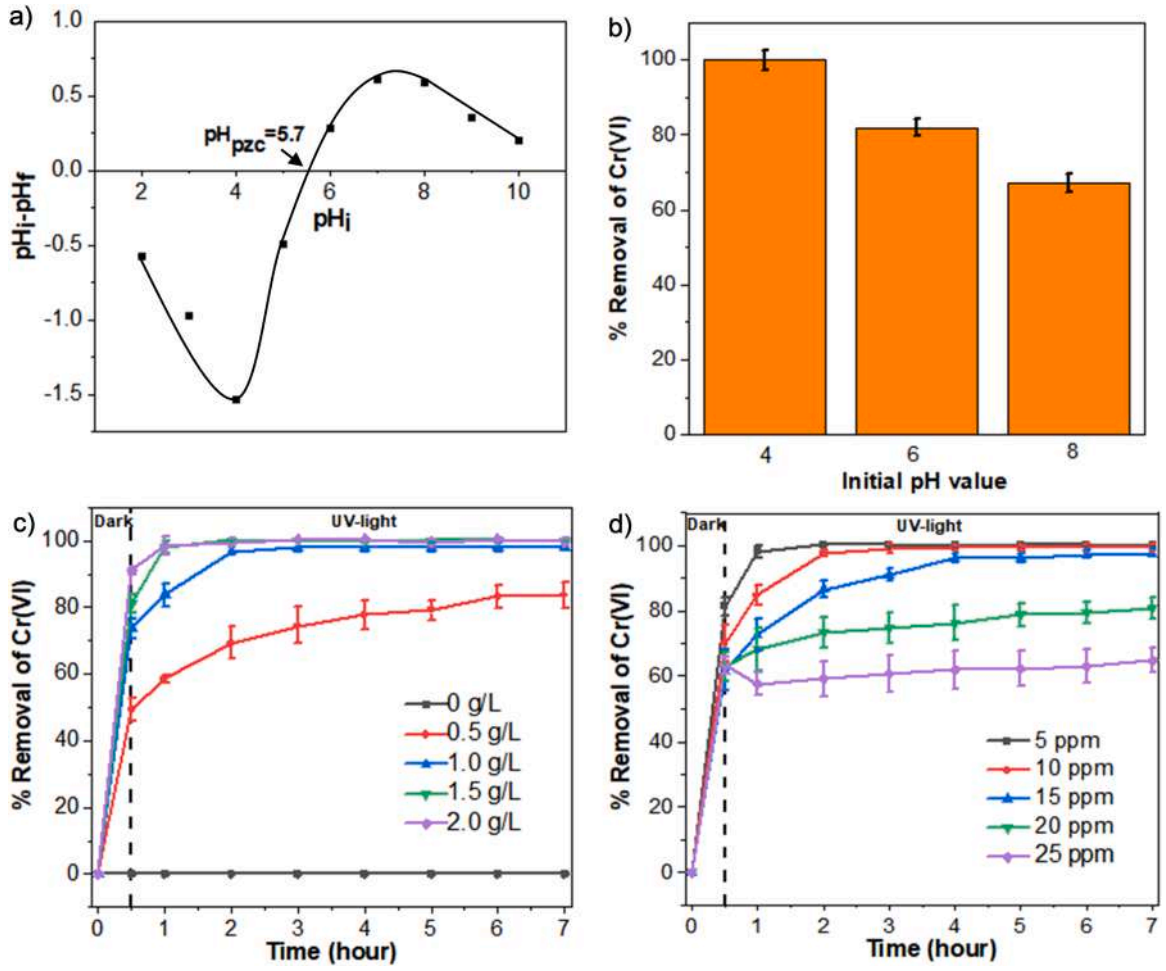

Fig. 8. a) pH_{pzc} of delaminated MXene, effect of various operating parameters on Cr(VI) removal at different, b)pH value (photocatalyst loading 1.5 g/L, Cr(VI) concentration 5 mg/L), c) photocatalyst loading (Cr(VI) concentration 5 mg/L) and d) initial concentration of Cr(VI) (photocatalyst loading 1.5 g/L).

stability and degradation.

On the other hand, the band gap energy (Eg) of the delaminated $Ti_3C_2T_x$ MXene was successfully estimated using the Kubelka–Munch function by plotting $(\alpha hv)^2$ versus hv, where α is the absorption coefficient and hv is the photon energy. As a result, the bandgap energy (Eg) of delaminated MXene was found at approximately 2.26 eV and greatly supported the photocatalytic ability under visible and UV light irradiation. This result also agrees with findings by [66,67] that reported the band gap energies of various functionalised Ti_3C_2 MXene were found to be in a range of 0.75–2.4 eV within the estimation of delaminated MXene of this study. (Fig. 5).

3.2. Synergistic effects of adsorption and photocatalysis

Fig. 6 compares the percentage (%) removal of Cr(VI) via adsorption and adsorption-assisted photocatalysis at different Cr(VI) concentrations. Based on the result, the adsorption process enhanced the removal of Cr(IV) during the adsorption-assisted photocatalysis process, in which the Cr(VI) removal was found to be higher for all targeted initial concentrations (5 mg/L–25 mg/L) with 3.1–28.9% of increment as compared to solely adsorption process. The synergistic effects of adsorption and photocatalysis greatly contributed to the excellent improvement of Cr(IV) removal under UV light irradiation.

In addition, as shown in Fig. 7, the adsorption activity demonstrated 81.2% removal at the initial 30 min. It reached 96.9% after 7 h of reaction under dark conditions, which corresponds to the equilibrium point. Under UV light irradiation, Cr(VI) removal by photocatalysis significantly improved to 97.9% within 30 min, exceeding the Cr(VI) removal without UV light after 7 h. The results reveal that delaminated MXene exhibited faster and higher Cr(VI) removal under UV light irradiation than without UV light irradiation, indicating the synergistic effect of adsorption and photocatalysis of delaminated MXene. It is noteworthy to mention that the removal efficiency of Cr(VI) by the delaminated MXene at optimal conditions achieved 100% and much better than several reported photocatalytic activity studies by other semiconducting photocatalysts; titanium dioxide P25 (50%) [68]; nanocomposite photocatalyst, Fe_3O_4 @$ZnCd_1$-xS (90%) [69]; and MOF-based photocatalyst, Zn-based MOF (95% and 96%) [70,71].

3.3. Performance evaluation for operating parameters

3.3.1. Effect of pH

The removal of heavy metal ions by adsorption and photocatalysis processes is affected by pH, as pH significantly affects the surface charge, diffusion process, and surface bindings of heavy metals [72]. The point of zero net charge or isoelectric point (pH_{pzc}) of delaminated MXene was determined by varying initial pH values (from 2 to 10) using HCl and NaOH. According to the plot of different pH changes, pH initial − pH final (pH_i-pH_f) versus pH initial (pH_i), the pH_{pzc} of delaminated MXene was approximately at pH 5.7 (Fig. 8a), which suggests delaminated MXene has a positive surface charge when pH of the solution is less than 5.7. In addition, Cr(VI) have different types of anionic forms depending on pH values. Cr(VI) commonly exists as $Cr_2O_7^{2-}$ and $HCrO_4^-$ under the acidic pH range, while under neutral and alkaline conditions, the

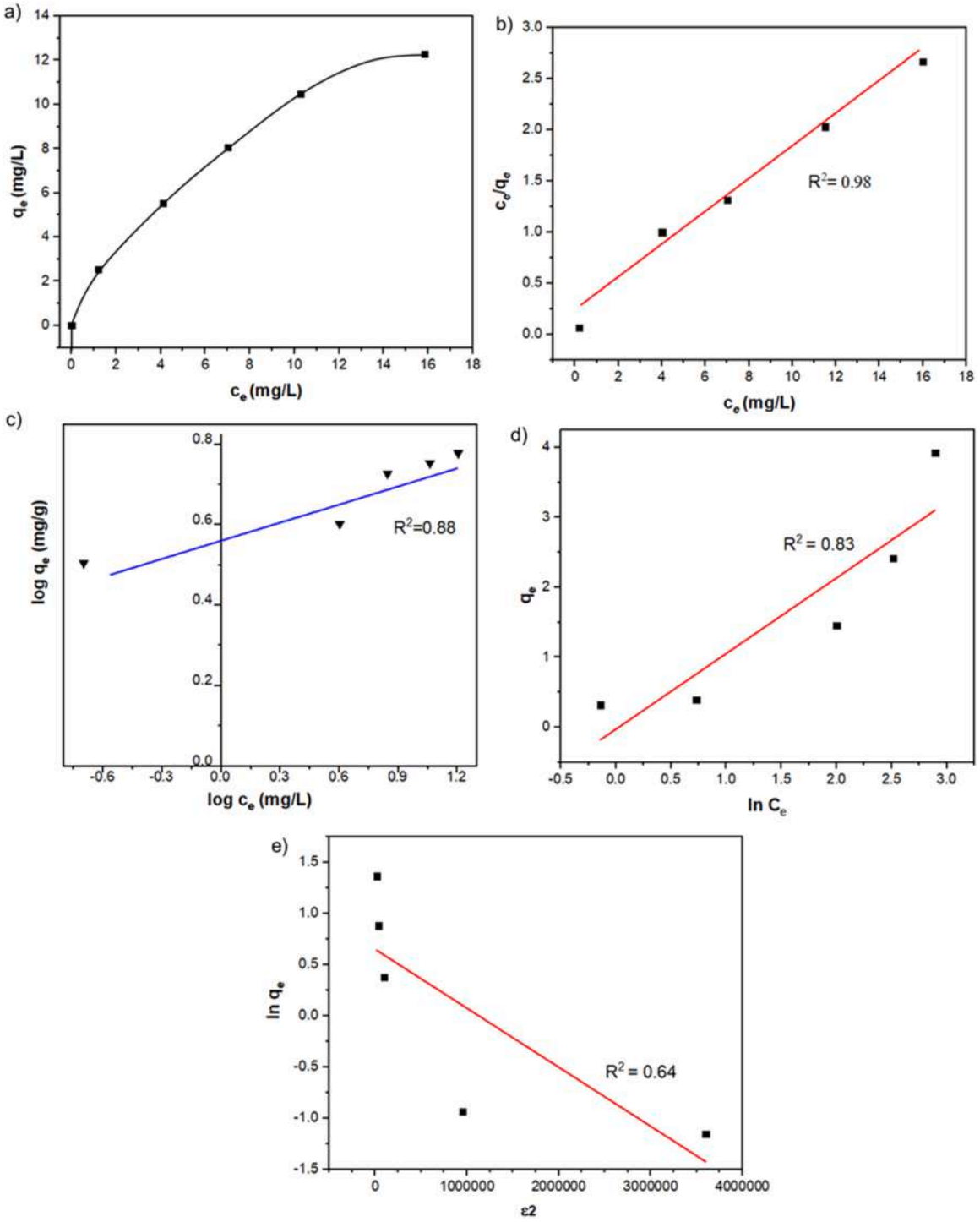

Fig. 9. (a) c_e versus q_e plot, (b) Langmuir isotherm and (c) Freundlich isotherm (d) Temkin isotherm (e) Dubinin–Radushkevich (D-R) isotherm models for Cr(VI) removal at different concentrations via adsorption under dark conditions.

dominant ionic form of Cr(VI) is CrO_4^{2-} [46].

The effect of initial pH on the removal of Cr(VI) was investigated at four different pH values (2, 4, 6, and 8). As shown in Fig. 8b, the removal of Cr(VI) decreased significantly from 100% to 67.1%, with increases in initial pH from 4 to 8. A similar trend was also observed during the adsorption of Cr(VI) under dark conditions after 7 h. This is possibly due to the electrostatic repulsion between the Cr(VI) metal ions and the surface charge of the synthesised delaminated MXene at a higher value of pH [73]. In contrast, at pH less than the pH_{pzc} value (5.7), the negative charge of OH^- in the delaminated MXene can be neutralised by positive H^+ ions, thus improving the removal of Cr(VI). These results are similar to a study reported for Cr(VI) removal by rice husk [72]. Nonetheless, when pH 2 of Cr(VI) was used, the Cr(VI) removal percentage decreased to 91%. Therefore, this finding concluded that pH 4 is the optimum pH condition for Cr(VI) removal using delaminated MXene via the synergistic adsorption-photocatalysis process.

3.3.2. *Effect of photocatalyst loading*

Direct photolysis without delaminated MXene exhibited no Cr(VI) removal for 7 h under UV irradiation. However, after 1.5 g/L of

Table 1
Adsorption capacities of Cr(VI) by different adsorbents at specific pH.

Adsorbent	pH	q_{max}	References
Graphene oxide	4	1.22 mg/g	[81]
Iron	4	1.27 mg/g	[82]
Zinc-Graphene oxide	4	3.67 mg/g	[83]
Titanium dioxide	3	23.8 mg/g	[84]
Activated alumina	2	7.44 mg/g	[85]
Guar gum-nano zinc oxide biocomposite		55.56 mg/g	[86]
Manganese oxide-coated sand grains		227.3 μg/g	[87]
Clay	2.5	1.50 mg/g	[88]
Delaminated MXene	4	6.25	Present work

Table 2
Calculated parameters of Langmuir and Freundlich, Temkin and Dubinin–Radushkevich (D-R) isotherm models.

Langmuir isotherm		**Freundlich isotherm**	
K_L (L/mg)	0.8744	K_F (mg/g) (L/mg) $^{(1/n)}$	3.8646
q_{max} (mg/g)	6.2841	$1/n$	0.1426
R^2	0.9848	R^2	0.8824
Temkin isotherm		**Dubinin–Radushkevich isotherm**	
B (J mol^{-1})	1.08148	Q_D (mg/g)	1.91625
A (L mg^{-1})	0.973946399	$\mathcal{E}$ (KJ/mol)	0.1426
R^2	0.8263	R^2	0.6374

delaminated MXene was added, the removal efficiency of Cr(VI) at equilibrium increased significantly to 100% due to sufficient active sites for Cr(VI) removal. Moreover, the increment of delaminated MXene loading up to 1.5 g/L caused the formation of excess free electrons in the conduction band and the escalation of free electrons and hydroxyl radicals on the delaminated MXene surface during photocatalysis [74]. Furthermore, this abundant surface-active site also facilitates effective interactions between the reactant and photocatalyst, thus enhancing the photocatalytic activity [75]. However, further increment of delaminated MXene to 2.0 g/L resulted in no further increment of Cr(VI) removal possibility due to the photocatalyst powder agglomeration that reduced the active sites on delaminated MXene, thus limiting the photocatalytic activity.

3.3.3. *Effect of Cr(VI) concentration*

The initial concentration of Cr(VI) is another operating parameter in the adsorption and photocatalysis experiment because it increases an osmotic pressure that drives the adsorption of a metal ion to an adsorbent surface from an aqueous solution [72]. The effect of initial Cr(VI) concentration on its removal efficiency by the adsorption-assisted photocatalytic process was evaluated by varying the initial Cr(VI)

Table 3
Pseudo-first-order and pseudo-second-order kinetic parameters.

Pseudo-first-order model			Pseudo-second-order model		
k_1 (min^{-1})	R^2	q_e (mg/g)	k_2 (g/mg•min)	R^2	q_e (mg/g)
− 0.000001	0.7595	2.00031	0.00042	0.9999	204.082
Intra-particle diffusion model			**Liquid film diffusion model**		
k_1 (g/mg min$^{0.5}$)	R^2	C	k_{id} (min^{-1})	R^2	
0.0085	0.8732	0.2986	0.7577	0.9659	

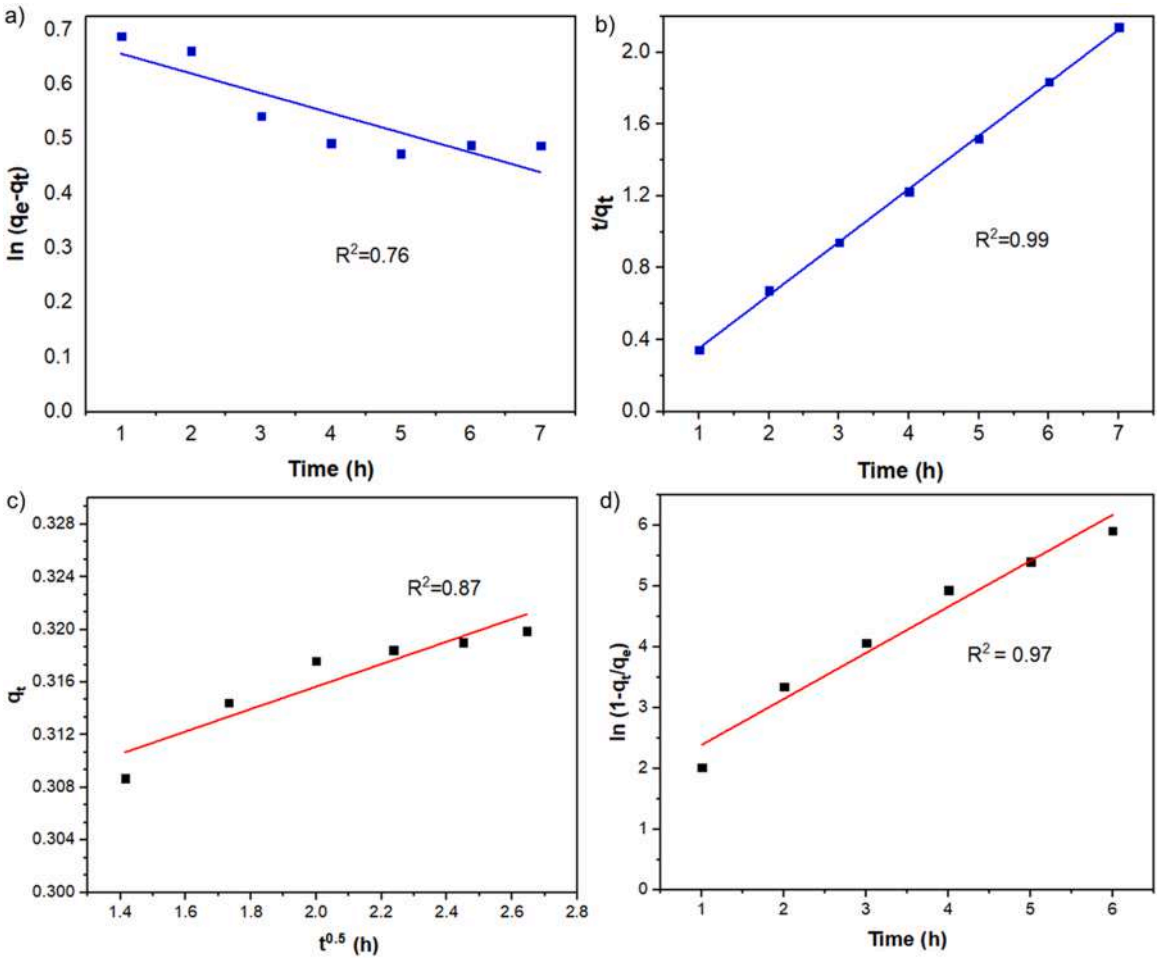

Fig. 10. (a) Pseudo-first-order and (b) pseudo-second-order (c) intraparticle diffusion and (d) film diffusion kinetic models for Cr(VI) removal via adsorption.

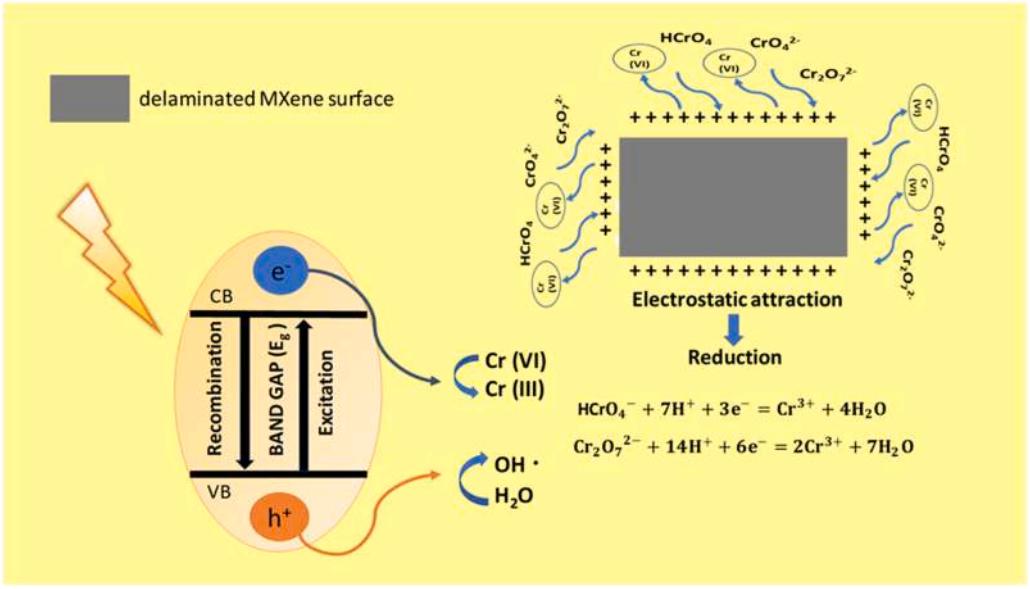

Scheme 3. Schematic illustration of the proposed mechanism for adsorption-assisted photocatalysis of Cr(VI) removal.

concentration from 5 to 25 mg/L. The equilibrium time for Cr(VI) removal is longer as the initial Cr(VI) concentration increases. The removal efficiency of Cr(VI) decreased from 100% to 64.9% with the increase of initial Cr(VI) concentrations from 5 to 25 mg/L. High initial Cr(VI) concentration resulted in the saturation of vacant sites on delaminated MXene, causing a further extension of the reaction time for a little improvement in pollutant removal [76,77]. Interestingly, even at a high concentration, the yellow colour of the initial Cr(VI) solution became more colourless after prolonging the reaction time, demonstrating the effectiveness of delaminated MXene on Cr(VI) removal. The effects of different pH, photocatalyst loading and initial concentrations are illustrated in Fig. 8(b, c and d).

3.4. Isotherm and kinetic analysis

The adsorption isotherms of Cr(VI) removal were calculated from the obtained adsorption results. Fig. 9(a) shows the c_e versus q_e plot; meanwhile, Fig. 9(b and c) illustrate the isotherms analysed using Freundlich and Langmuir isotherm models. The linear plot of the Langmuir isotherm model ($c_e$versus c_e/q_e) (R^2 = 0.98) gave a better agreement with experimental data as compared to the Freundlich isotherm model (R^2 = 0.88). According to the Langmuir model, the Cr (VI) removal mechanism was attributed to the physical and monolayer adsorption [72,78]. Langmuir isotherm also suggests that the monolayer site energy of adsorption properties on the adsorbent surface is equal and saturated after the monolayer adsorption [79,80]. The removal efficiency and q_{max} of 6.28 mg/g Cr(VI) obtained in the Langmuir isotherm are comparable to other reported adsorbents such as activated carbon, activated charcoal, graphene oxide, Zn-graphene oxide and iron, as shown in Table 1. Therefore, this study proved that the synthesised delaminated MXene demonstrated a potential adsorbent for Cr(VI) removal in aqueous. In addition, the Temkin and Dubinin–Radushkevich (D-R) isotherm models were also analysed in this study. Fig. 9(d and e) show a lower regression coefficient of both Temkin (R^2 = 0.83) and Dubinin–Radushkevich (D-R) (R^2 = 0.64) isotherms as compared to Langmuir and Freundlich isotherms indicating these models did not satisfactorily fit the adsorption data of Cr(VI) removal. Overall, it can be seen that the best adsorption isotherm was described by the Langmuir model, followed by Temkin, Freundlich and Dubinin–Radushkevich (D-R) isotherm models as tabulated in Table 2.

The kinetics of the adsorption process was analysed using pseudo-first- and pseudo-second-order models. Fig. 10 (a and b) show the pseudo-first-order and pseudo-second-order models for Cr(VI) removal. The pseudo-second-order model displayed a better agreement than the pseudo-first-order model. This result suggests that the removal of Cr(VI) was controlled by the chemisorption process involving the electron exchange that provides a fast adsorption rate of pollutants [72,79,89]. Several works also reported the same findings on the removal of Cr(VI) onto different types of adsorbent/photocatalyst, such as chitosan/g-C_3N_4/TiO_2 [79] and graphene/g-C_3N_4 [90]. The pseudo-first-order and pseudo-second-order kinetic parameters are summarised in Table 3.

In addition, the diffusion rate-controlling steps for Cr(VI) removal were elucidated using the intraparticle diffusion and liquid film diffusion models following the equations reported by [56]. Fig. 10 (c) shows the straight-line plot of q_t versus $t^{0.5}$ does not pass the origin point (R^2 = 0.87), indicating that the adsorption process was not dominantly controlled by intraparticle diffusion. In contrast, a higher regression coefficient in the liquid film model (Fig. 10 d) (R^2 = 0.97) would suggest that the kinetics of the adsorption process is diffusion controlled. Thus, it is suggested that the transport of the Cr(VI) sorbate molecules is controlled by diffusion through the liquid film surrounding the solid adsorbent.

3.5. Proposed mechanism of Cr(VI) removal

The possible mechanism for adsorption-assisted photocatalysis of Cr (VI) removal is proposed and illustrated in Scheme 3. As the pH of Cr(VI) is less than pH_{pzc} value= 5.7, the C═O and −OH on the delaminated MXene surface protonate with H^+, forming a positively charged surface which attracts the negatively charged Cr(VI) via electrostatic interaction mechanism. On the other hand, at the pH range of 2–6, Cr(VI) mainly exists as $HCrO_4^-$, which can enhance the electrostatic attraction between Cr(VI) anions and the positively charged surface of the adsorbent. The subsequent mechanism under UV irradiation can be well described by photocatalytic reduction.

The charge generation takes place when the UV light irradiation interacts with delaminated MXene prior to receiving energy similar to or higher than its band gap energy (Eq. 9), causing the electrons of delaminated MXene to excite from the valence band (VB) to the conduction band (CB), forming electron-hole pairs (e^-–h^+) (Eq. 10). As a result, the generated electron-hole pairs, which migrate to the photocatalyst surface, initiated the photocatalytic reactions, and further reacted with water to generate oxygen and hydrogen ions (Eq. 10). Since

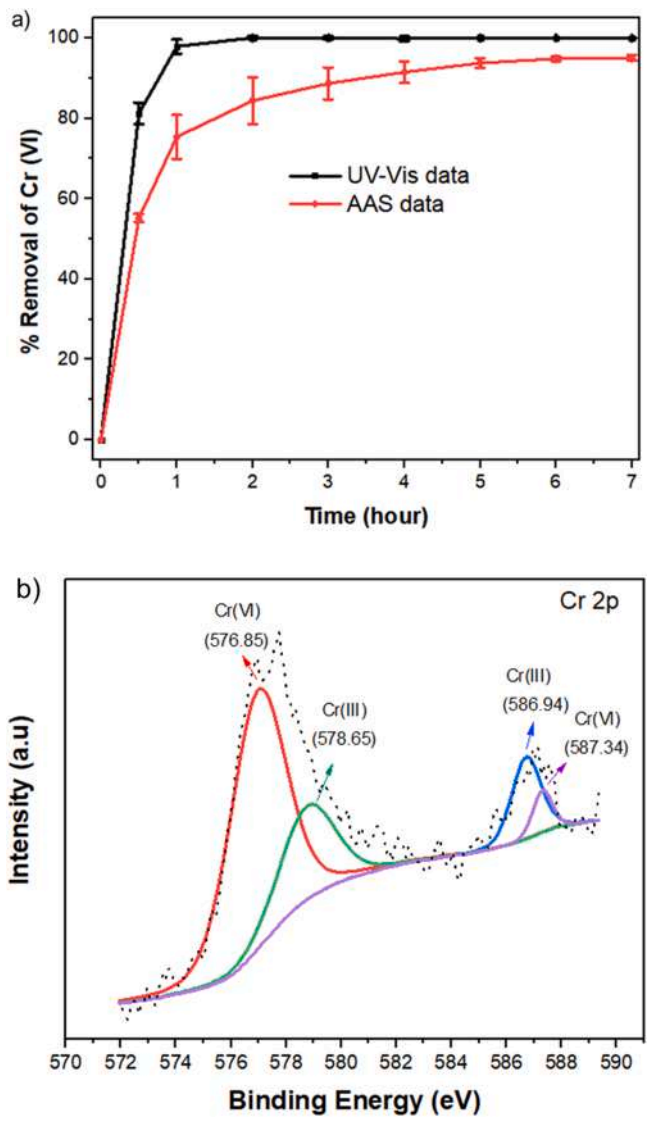

Fig. 11. a) Percentage of Cr(IV) using AAS and UV-Vis spectroscopy and b) XPS spectra of Cr 2p peak on delaminated MXene after adsorption-assisted photocatalysis process.

there is no electron scavenger involved, Cr(VI) ions serve as the photoelectron acceptor and react with the photogenerated electrons of delaminated MXene and thus reduce Cr(VI) to Cr(III) (Eq. 11 and Eq. 12). In addition, the holes may also lead to the generation of O_2 (Eq. 8) in the absence of organics [91]. The overall Cr(VI) reduction process at (pH = 4–6) in this study can be expressed by the following equations (Eqs 9–12) [79]:

$$Ti_3C_2T_x + hv + 3e^- \rightarrow h^+ + e^- \quad (9)$$

$$2H_2O + 4H^+ + 3e^- \rightarrow O_2 + 4H^+ \quad (10)$$

$$HCrO_4^- + 7H^+ + 3e^- \rightarrow Cr^{3+} + 4H_2O \quad (11)$$

$$Cr_2O_7^{2-} + 14H^+ + 6e^- \rightarrow 2Cr^{3+} + 7H_2O \quad (12)$$

The mechanism of Cr(IV) removal via adsorption-assisted photocatalysis can be further verified through the reduction of Cr(VI) to Cr (III). In this study, atomic absorption spectroscopy (AAS) detected the amount of Cr(VI) regardless of its changes in oxidation state. Meanwhile, the ultraviolet-visible (UV-Vis) spectrophotometer detected Cr(VI) at a UV absorbance of 543 nm. The Cr(III) concentration was obtained by subtracting the Cr(VI) concentration using a UV-Vis spectrophotometer from the total Cr based on AAS measurement. The trend of Cr(VI) reduction to Cr(III) can be seen in Fig. 11a. Based on the results, the Cr (VI) removal rate increased rapidly after the Cr(VI) solution was irradiated under UV light. To further confirm the reduction of Cr(VI), the XPS spectrum of Cr 2p after the reaction was analysed (Fig. 11b). Two significant peaks originating from Cr $2p_{3/2}$ and Cr $2p_{1/2}$ orbitals revealed binding energy bands occurring at around 576.85, 587.34 and 578.65, 586.94, which can be assigned to the higher oxidation state of Cr, Cr(VI) and lower oxidation state of Cr, Cr(III), respectively [92].

On the other hand, the XPS spectra of fresh delaminated MXene in Fig. 3 were also compared with the delaminated MXene after reaction (Fig. 12) to investigate the changes in the chemical state of delaminated MXene before and after Cr(VI) removal. It was found that the binding energy of Ti_2p of TiO_2 shifted from (459.18) to a lower value of 458.80, illustrating that the proportion of Ti_3+ becomes larger after the reaction. Generally, the shifting of Ti_2p was due to the accumulation of defective TiO_2 [93]. The presence of TiO_2 showed that $Ti_3C_2T_x$ particles reacted in Cr(VI) solution and formed TiO_2 on its surface, decreasing the Ti_3C_2 signal. The XPS spectrum can be verified in C 1 s and O 1 s regions. The high peak of C-O after reaction showed binding of Ti-C reduced to C-O. The oxidation of $Ti_3C_2T_x$ into Ti oxides was plausibly due to the interaction between $Ti_3C_2T_x$, Cr(VI), water (H_2O) and Oxygen(O_2).

Moreover, it has been experimentally confirmed that the presence of TiO_2 in MXene was influenced by the oxygen dissolved in water that acts as an oxidising agent [94]. As a result, the oxidation of $Ti_3C_2T_x$ layers

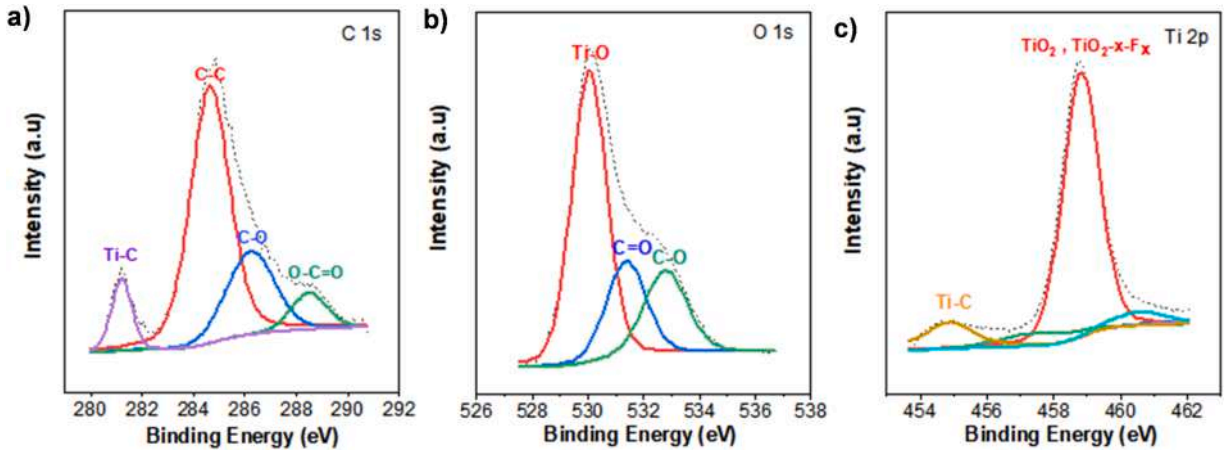

Fig. 12. XPS spectra of delaminated MXene after Cr(VI) removal.

into nanoscale TiO_2 may increase the accessible photoresponse capacity, especially under light irradiation. This finding was similar to other reported studies on MXene/g-C_3N_4 photocatalyst [95]. However, future research needs to be conducted to further understand the MXene stability in an aqueous solution for a prolonged reaction time.

4. Conclusion

This study successfully synthesised delaminated MXene by etching the MAX phase of Ti_3AlC_2. The Cr(VI) removal of the delaminated MXene via adsorption-assisted photocatalysis was investigated by evaluating the effect of pH, delaminated MXene loading, and initial concentration of Cr(VI). The experimental work demonstrated that the best photocatalyst loading and initial Cr(VI) concentration were 1.5 g/L and 5 mg/L, respectively. Furthermore, the Cr(VI) removal reached 100% under UV light irradiation only within 3 h reaction time, whereas simple adsorption achieved approximately 96.9% removal after 7 h. Overall, the adsorption-assisted photocatalysis process exhibited approximately 28.9% higher Cr(VI) removal efficiency than adsorption. Such excellent performance was attributed to the synergistic effect of electrostatic attraction of delaminated MXene surface with Cr(VI) ions and photogenerated conduction band electrons in delaminated MXene under UV light irradiation. The Langmuir model best fits the equilibrium isotherm, confirming that the adsorption of Cr(VI) was due to the monolayer sorption processes. The pseudo-second-order kinetic model further described the time dependence on Cr(VI) sorption. The detailed mechanism for adsorption-assisted photocatalysis of Cr(VI) by delaminated MXene was proposed and demonstrated that delaminated MXene has potential as an excellent photocatalytic adsorbent for removing Cr (VI) from an aqueous solution. However, the application of $Ti_3C_2T_X$ delaminated MXene in this study still needs further investigation, especially in terms of stability and reusability of the photocatalyst. Further research should also focus on the oxidation stability of delaminated MXene in an aqueous liquid and at room temperature.

Furthermore, the stability of MXene could also be improved by combining MXene with other semiconductor materials. In addition, the effects of other parameters during photocatalysis, such as the presence of inorganic anions and hole scavengers, need to be further explored. Lastly, the performance of Cr(VI) removal by the synthesised delaminated MXene should also be evaluated on the bigger scale of industrial wastewater.

CRediT authorship contribution statement

Nur Shafiqah Jamaluddin: Run the lab works, data curation and writing – original draft preparation, **Nur Hashimah Alias:** Supervision, Writing – original draft preparation, reviewing and editing., **Sadaki Samitsu:** Writing – original draft preparation and reviewing, **Nur Hidayati Othman:** Conceptualization, Methodology, **Juhana Jaafar:** Supervision, Methodology, **Fauziah Marpani:** Methodology, **Woei Jye Lau:** Conceptualization, **Yong Zen Tan:** Reviewing and editing the final manuscript.

Declaration of Competing Interest

The authors declare that they have no known competing financial interests or personal relationships that could have appeared to influence the work reported in this paper.

Data availability

Data will be made available on request.

Acknowledgements

The authors gratefully acknowledged the Ministry of Higher Education Malaysia (MOHE) for the FRGS research funding (600-IRMI/FRGS 5/3 (441/2019)). N.S.J., N.H.A and J.J. would also like to thank the Advanced Membrane Technology Research Centre (AMTEC), Universiti Teknologi Malaysia (UTM), Malaysia, for the awarded AMTEC fellowship.

References

[1] H. Li, N. Li, P. Zuo, S. Qu, W. Shen, Efficient adsorption-reduction synergistic effects of sulfur, nitrogen and oxygen heteroatom co-doped porous carbon spheres for chromium(VI) removal, Colloids Surf. A Physicochem. Eng. Asp. 618 (2021), 126502, https://doi.org/10.1016/j.colsurfa.2021.126502.

[2] R.F.S. Barbosa, A.G. Souza, H.F. Maltez, D.S. Rosa, Chromium removal from contaminated wastewaters using biodegradable membranes containing cellulose nanostructures, Chem. Eng. J. 395 (2020), 125055, https://doi.org/10.1016/j.cej.2020.125055.

[3] V.T. Trang, L.T. Tam, N. Van Quy, V.N. Phan, H. Van Tuan, T.Q. Huy, N.X. Dinh, A. T. Le, Enhanced adsorption efficiency of inorganic chromium (VI) ions by using carbon-encapsulated hematite nanocubes, J. Sci. Adv. Mater. Devices 5 (2020) 392–399, https://doi.org/10.1016/j.jsamd.2020.05.007.

[4] H. Liang, B. Song, P. Peng, G. Jiao, X. Yan, D. She, Preparation of three-dimensional honeycomb carbon materials and their adsorption of Cr(VI, Chem. Eng. J. 367 (2019) 9–16, https://doi.org/10.1016/j.cej.2019.02.121.

[5] J. Zhou, Y. Wang, J. Wang, W. Qiao, D. Long, L. Ling, Effective removal of hexavalent chromium from aqueous solutions by adsorption on mesoporous carbon microspheres, J. Colloid Interface Sci. 462 (2016) 200–207, https://doi.org/10.1016/j.jcis.2015.10.001.

[6] Y. Tadjenant, N. Dokhan, A. Barras, A. Addad, R. Jijie, S. Szunerits, R. Boukherroub, Graphene oxide chemically reduced and functionalized with KOH-PEI for efficient Cr(VI) adsorption and reduction in acidic medium, Chemosphere 258 (2020), 127316, https://doi.org/10.1016/j.chemosphere.2020.127316.

[7] G. Chen, H. Liu, Photochemical removal of hexavalent chromium and nitrate from ion-exchange brine waste using carbon-centered radicals, Chem. Eng. J. 396 (2020), 125136, https://doi.org/10.1016/j.cej.2020.125136.

[8] Y. Xie, J. Lin, J. Liang, M. Li, Y. Fu, H. Wang, S. Tu, J. Li, Hypercrosslinked mesoporous poly(ionic liquid)s with high density of ion pairs: efficient adsorbents for Cr(VI) removal via ion-exchange, Chem. Eng. J. 378 (2019), 122107, https://doi.org/10.1016/j.cej.2019.122107.

[9] B. Xie, C. Shan, Z. Xu, X. Li, X. Zhang, J. Chen, B. Pan, One-step removal of Cr(VI) at alkaline pH by UV/sulfite process: Reduction to Cr(III) and in situ Cr(III) precipitation, Chem. Eng. J. 308 (2017) 791–797, https://doi.org/10.1016/j.cej.2016.09.123.

[10] S. Koushkbaghi, A. Zakialamdari, M. Pishnamazi, H.F. Ramandi, M. Aliabadi, M. Irani, Aminated-Fe3O4 nanoparticles filled chitosan/PVA/PES dual layers nanofibrous membrane for the removal of Cr(VI) and Pb(II) ions from aqueous solutions in adsorption and membrane processes, Chem. Eng. J. 337 (2018) 169–182, https://doi.org/10.1016/j.cej.2017.12.075.

[11] H. Semghouni, S. Bey, A. Figoli, A. Criscuoli, M. Benamor, E. Drioli, Chromium (VI) removal by Aliquat-336 in a novel multiframe flat sheet membrane contactor, Chem. Eng. Process. - Process. Intensif. 147 (2020), 107765, https://doi.org/10.1016/j.cep.2019.107765.

[12] S. Zhao, Z. Chen, J. Shen, Y. Qu, B. Wang, X. Wang, Enhanced Cr(VI) removal based on reduction-coagulation-precipitation by NaBH4 combined with fly ash leachate as a catalyst, Chem. Eng. J. 322 (2017) 646–656, https://doi.org/10.1016/j.cej.2017.04.057.

[13] L. Xiang, C.G. Niu, N. Tang, X.X. Lv, H. Guo, Z.W. Li, H.Y. Liu, L.S. Lin, Y.Y. Yang, C. Liang, Polypyrrole coated molybdenum disulfide composites as adsorbent for enhanced removal of Cr(VI) in aqueous solutions by adsorption combined with reduction, Chem. Eng. J. 408 (2021), 127281, https://doi.org/10.1016/j.cej.2020.127281.

[14] J. Sun, Y. Hou, Z. Yu, L. Tu, Y. Yan, S. Qin, S. Chen, D. Lan, H. Zhu, S. Wang, Visible-light-driven Z-scheme Zn3In2S6/AgBr photocatalyst for boosting simultaneous Cr (VI) reduction and metronidazole oxidation: kinetics, degradation pathways and mechanism, J. Hazard. Mater. (2021), 126543, https://doi.org/10.1016/j.jhazmat.2021.126543.

[15] Y. Liu, D. Yang, T. Xu, Y. Shi, L. Song, Z.Z. Yu, Continuous photocatalytic removal of chromium (VI) with structurally stable and porous Ag/Ag3PO4/reduced graphene oxide microspheres, Chem. Eng. J. 379 (2020), 122200, https://doi.org/10.1016/j.cej.2019.122200.

[16] D. Lu, P. Fang, W. Wu, J. Ding, L. Jiang, X. Zhao, C. Li, M. Yang, Y. Li, D. Wang, Solvothermal-assisted synthesis of self-assembling TiO2 nanorods on large graphitic carbon nitride sheets with their anti-recombination in the photocatalytic removal of Cr(VI) and rhodamine B under VIsible light irradiation, Nanoscale 9 (2017) 3231–3245, https://doi.org/10.1039/c6nr09137g.

[17] L.W. Duresa, D.H. Kuo, K.E. Ahmed, M.A. Zeleke, H. Abdullah, Highly enhanced photocatalytic Cr(vi) reduction using In-doped Zn(O,S) nanoparticles, N. J. Chem. 43 (2019) 8746–8754, https://doi.org/10.1039/c9nj01511f.

[18] M. Rosales, A. Garcia, V.M. Fuenzalida, R. Espinoza-González, G. Song, B. Wang, J. Yu, F. Gracia, A. Rosenkranz, Unprecedented arsenic photo-oxidation behavior of few- and multi-layer Ti3C2Tx nano-sheets, Appl. Mater. Today 20 (2020), 100769, https://doi.org/10.1016/j.apmt.2020.100769.

[19] M. Azuwa, J. Jaafar, M.F.M. Zain, L. Jeffery, M.B. Kassim, M. Saufi, N. Hashimah, In-depth understanding of core-shell nanoarchitecture evolution of g-C3N4@C,N

co-doped anatase/rutile: Efficient charge separation and enhanced visible-light photocatalytic performance, Appl. Surf. Sci. 436 (2018) 302–318.
[20] D. Hussain, M.F. Siddiqui, Z. Shirazi, T.A. Khan, Evaluation of adsorptive and photocatalytic degradation properties of FeWO4/polypyrrole nanocomposite for rose bengal and alizarin red S from liquid phase: modeling of adsorption isotherms and kinetics data, Environ. Prog. Sustain. Energy (2022), e13822, https://doi.org/10.1002/EP.13822.
[21] C. Santhosh, A. Malathi, E. Daneshvar, P. Kollu, A. Bhatnagar, Photocatalytic degradation of toxic aquatic pollutants by novel magnetic 3D-TiO2@HPGA nanocomposite, 8, Sci. Rep. 2018 (81) (2018) 1–15, https://doi.org/10.1038/s41598-018-33818-9.
[22] Y. Yang, L. Yan, J. Li, J. Li, T. Yan, M. Sun, Z. Pei, Synergistic adsorption and photocatalytic reduction of Cr(VI) using Zn-Al-layered double hydroxide and TiO2 composites, Appl. Surf. Sci. 492 (2019) 487–496, https://doi.org/10.1016/j.apsusc.2019.06.229.
[23] Q. Xia, B. Huang, X. Yuan, H. Wang, Z. Wu, L. Jiang, T. Xiong, J. Zhang, G. Zeng, H. Wang, Modified stannous sulfide nanoparticles with metal-organic framework: Toward efficient and enhanced photocatalytic reduction of chromium (VI) under visible light, J. Colloid Interface Sci. 530 (2018) 481–492, https://doi.org/10.1016/j.jcis.2018.05.015.
[24] C.R. Chen, H.Y. Zeng, S. Xu, J.C. Shen, G. Hu, R.L. Zhu, J.Z. Du, Y.X. Sun, Facile fabrication of CdS/ZnAlO heterojunction with enhanced photocatalytic activity for Cr(VI) reduction under visible light, Appl. Clay Sci. 165 (2018) 197–204, https://doi.org/10.1016/j.clay.2018.08.019.
[25] Z. Chen, Y. Luo, C. Huang, X. Shen, In situ assembly of ZnO/graphene oxide on synthetic molecular receptors: towards selective photoreduction of Cr(VI) via interfacial synergistic catalysis, Chem. Eng. J. 414 (2021), 128914, https://doi.org/10.1016/j.cej.2021.128914.
[26] Y. Sun, L. Xu, P. Jin, X. Bai, X. Jin, X. Shi, Simultaneous removal of colorless micropollutants and hexavalent chromium by pristine TiO2 under visible light: An electron transfer mechanism, Chem. Eng. J. 405 (2021), 126968, https://doi.org/10.1016/j.cej.2020.126968.
[27] L. Hou, Y. Zhang, Y. Ma, Y. Wang, Z. Hu, Y. Gao, Z. Han, Reduced phosphomolybdate hybrids as efficient visible-light photocatalysts for Cr(VI) reduction, Inorg. Chem. 58 (2019) 16667–16675, https://doi.org/10.1021/acs.inorgchem.9b02777.
[28] M. Naguib, M. Kurtoglu, V. Presser, J. Lu, J. Niu, M. Heon, L. Hultman, Y. Gogotsi, M.W. Barsoum, Two-dimensional nanocrystals produced by exfoliation of Ti3AlC2, Adv. Mater. 23 (2011) 4248–4253, https://doi.org/10.1002/adma.201102306.
[29] M. Alhabeb, K. Maleski, B. Anasori, P. Lelyukh, L. Clark, S. Sin, Y. Gogotsi, Guidelines for synthesis and processing of two-dimensional titanium carbide (Ti3C2Tx MXene), Chem. Mater. 29 (2017) 7633–7644, https://doi.org/10.1021/acs.chemmater.7b02847.
[30] X. Feng, Z. Yu, Y. Sun, R. Long, M. Shan, X. Li, Y. Liu, J. Liu, Review MXenes as a new type of nanomaterial for environmental applications in the photocatalytic degradation of water pollutants, Ceram. Int (2020), https://doi.org/10.1016/j.ceramint.2020.11.151.
[31] C. Prasad, X. Yang, Q. Liu, H. Tang, A. Rammohan, S. Zulfiqar, G.V. Zyryanov, S. Shah, Recent advances in MXenes supported semiconductors based photocatalysts: Properties, synthesis and photocatalytic applications, J. Ind. Eng. Chem. 85 (2020) 1–33, https://doi.org/10.1016/j.jiec.2019.12.003.
[32] B. Sun, P. Qiu, Z. Liang, Y. Xue, X. Zhang, L. Yang, H. Cui, J. Tian, The fabrication of 1D/2D CdS nanorod@Ti3C2 MXene composites for good photocatalytic activity of hydrogen generation and ammonia synthesis, Chem. Eng. J. 406 (2021), 127177, https://doi.org/10.1016/j.cej.2020.127177.
[33] Y. Ying, Y. Liu, X. Wang, Y. Mao, W. Cao, P. Hu, X. Peng, Two-dimensional titanium carbide for efficiently reductive removal of highly toxic chromium(VI) from water, ACS Appl. Mater. Interfaces 7 (2015) 1795–1803, https://doi.org/10.1021/am5074722.
[34] Z. Li, Y. Wu, 2D early transition metal carbides (MXenes) for Catalysis, Small 15 (2019), 1804736, https://doi.org/10.1002/SMLL.201804736.
[35] H. Wang, Y. Sun, Y. Wu, W. Tu, S. Wu, X. Yuan, G. Zeng, Z.J. Xu, S. Li, J.W. Chew, Electrical promotion of spatially photoinduced charge separation via interfacial-built-in quasi-alloying effect in hierarchical Zn2In2S5/Ti3C2(O, OH)x hybrids toward efficient photocatalytic hydrogen evolution and environmental remediation, Appl. Catal. B Environ. 245 (2019) 290–301, https://doi.org/10.1016/j.apcatb.2018.12.051.
[36] J. Lao, R. Lv, J. Gao, A. Wang, J. Wu, J. Luo, Aqueous Stable Ti 3C 2 MXene membrane with fast and photoswitchable nanofluidic transport, ACS Nano 12 (2018) 12464–12471, https://doi.org/10.1021/acsnano.8b06708.
[37] S. Kim, M. Yu, Y. Yoon, Fouling and retention mechanisms of selected cationic and anionic dyes in a Ti3C2Tx MXene-ultrafiltration hybrid system, ACS Appl. Mater. Interfaces 12 (2020) 16557–16565, https://doi.org/10.1021/acsami.0c02454.
[38] B. Zielińska, A. Wróblewska, K. Maślana, P. Miądlicki, K. Kiełbasa, A. Rozmysłowska-Wojciechowska, M. Petrus, J. Woźniak, A.M. Jastrzębska, B. Michalkiewicz, E. Mijowska, High catalytic performance of 2D Ti3C2Tx MXene in α-pinene isomerization to camphene, Appl. Catal. A Gen. 604 (2020), 117765, https://doi.org/10.1016/j.apcata.2020.117765.
[39] V. Sharma, A. Kumar, A. Kumar, V. Krishnan, Enhanced photocatalytic activity of two dimensional ternary nanocomposites of ZnO–Bi2WO6–Ti3C2 MXene under natural sunlight irradiation, Chemosphere 287 (2022), https://doi.org/10.1016/J.CHEMOSPHERE.2021.132119.
[40] P. Kuang, J. Low, B. Cheng, J. Yu, J. Fan, MXene-based photocatalysts, J. Mater. Sci. Technol. 56 (2020) 18–44, https://doi.org/10.1016/j.jmst.2020.02.037.
[41] L. Zhang, P. Ma, L. Dai, S. Li, W. Yu, J. Guan, In situ crystallization and growth of TiO2 nanospheres between MXene layers for improved adsorption and visible light photocatalysis, Catal. Sci. Technol. 11 (2021) 3834–3844, https://doi.org/10.1039/D1CY00239B.
[42] A. Shahzad, K. Rasool, W. Miran, M. Nawaz, J. Jang, K.A. Mahmoud, D.S. Lee, Two-Dimensional Ti3C2Tx MXene Nanosheets for Efficient Copper Removal from Water, ACS Sustain, Chem. Eng. 5 (2017) 11481–11488, https://doi.org/10.1021/acssuschemeng.7b02695.
[43] Q. Peng, J. Guo, Q. Zhang, J. Xiang, B. Liu, A. Zhou, R. Liu, Y. Tian, Unique lead adsorption behavior of activated hydroxyl group in two-dimensional titanium carbide, J. Am. Chem. Soc. 136 (2014) 4113–4116, https://doi.org/10.1021/ja500506k.
[44] A. Shahzad, K. Rasool, W. Miran, M. Nawaz, J. Jang, K.A. Mahmoud, D.S. Lee, Mercuric ion capturing by recoverable titanium carbide magnetic nanocomposite, J. Hazard. Mater. 344 (2018) 811–818, https://doi.org/10.1016/j.jhazmat.2017.11.026.
[45] K. Fu, X. Liu, D. Yu, J. Luo, Z. Wang, J.C. Crittenden, Highly efficient and selective Hg(II) removal from water using multilayered Ti3C2O xMXene via adsorption coupled with catalytic reduction mechanism, Environ. Sci. Technol. 54 (2020) 16212–16220, https://doi.org/10.1021/acs.est.0c05532.
[46] P. Karthikeyan, K. Ramkumar, K. Pandi, A. Fayyaz, S. Meenakshi, C.M. Park, Effective removal of Cr(VI) and methyl orange from the aqueous environment using two-dimensional (2D) Ti3C2Tx MXene nanosheets, Ceram. Int. 47 (2021) 3692–3698, https://doi.org/10.1016/J.CERAMINT.2020.09.221.
[47] Y. Tang, C. Yang, W. Que, A novel two-dimensional accordion-like titanium carbide (MXene) for adsorption of Cr(VI) from aqueous solution, J. Adv. Dielectr. 8 (2018), 1850035, https://doi.org/10.1142/S2010135×18500352.
[48] A. Kong, Y. Sun, M. Peng, H. Gu, Y. Fu, J. Zhang, W. Li, Amino-functionalized MXenes for efficient removal of Cr(VI, Colloids Surf. A Physicochem. Eng. Asp. 617 (2021), 126388, https://doi.org/10.1016/j.colsurfa.2021.126388.
[49] O. Mashtalir, K.M. Cook, V.N. Mochalin, M. Crowe, M.W. Barsoum, Y. Gogotsi, Dye adsorption and decomposition on two-dimensional titanium carbide in aqueous media, J. Mater. Chem. A. 2 (2014) 14334–14338, https://doi.org/10.1039/C4TA02638A.
[50] D. Zhao, C. Cai, Preparation of Bi2MoO6/Ti3C2MXene heterojunction photocatalysts for fast tetracycline degradation and Cr(vi) reduction, Inorg. Chem. Front. 7 (2020) 2799–2808, https://doi.org/10.1039/d0qi00540a.
[51] G. Zou, Z. Zhang, J. Guo, B. Liu, Q. Zhang, C. Fernandez, Q. Peng, Synthesis of MXene/Ag composites for extraordinary long cycle lifetime lithium storage at high rates, ACS Appl. Mater. Interfaces 8 (2016) 22280–22286, https://doi.org/10.1021/acsami.6b08089.
[52] N.H. Alias, J. Jaafar, S. Samitsu, N. Yusof, M. Hafiz, D. Othman, M.A. Rahman, A. Fauzi Ismail, F. Aziz, W. Norharyati, W. Salleh, N.H. Othman, Photocatalytic degradation of oilfield produced water using graphitic carbon nitride embedded in electrospun polyacrylonitrile nanofibers, Chemosphere 204 (2018) 79–86, https://doi.org/10.1016/j.chemosphere.2018.04.033.
[53] P. Makuła, M. Pacia, W. Macyk, How to correctly determine the band gap energy of modified semiconductor photocatalysts based on UV-Vis, Spectra, J. Phys. Chem. Lett. 9 (2018) 6814–6817, https://doi.org/10.1021/ACS.JPCLETT.8B02892/SUPPL_FILE/JZ8B02892_LIVESLIDES.MP4.
[54] A. Lace, D. Ryan, M. Bowkett, J. Cleary, Chromium monitoring in water by colorimetry using optimised 1,5-diphenylcarbazide method, Int. J. Environ. Res. Public Health 16 (2019), https://doi.org/10.3390/IJERPH16101803.
[55] T. Tarawou, D. Wankasi, M.H. Jnr, Equilibrium sorption studies of basic blue-9 dye from aqueous medium using activated carbon produced from water hyacinth (Eichornia crassipes,), J. Nepal Chem. Soc. 29 (2013) 67–74, https://doi.org/10.3126/jncs.v29i0.9254.
[56] T.A. Khan, S. Sharma, I. Ali, Adsorption of Rhodamine B dye from aqueous solution onto acid activated mango (Magnifera indica) leaf powder: Equilibrium, Kinet. Thermodyn. Stud., J. Toxicol. Environ. Heal. Sci. 3 (2011) 286–297. ⟨http://www.academicjournals.org/article/article1379597780_Khanetal.pdf⟩.
[57] C. Peng, P. Wei, X. Chen, Y. Zhang, F. Zhu, Y. Cao, H. Wang, H. Yu, F. Peng, A hydrothermal etching route to synthesis of 2D MXene (Ti3C2, Nb2C): Enhanced exfoliation and improved adsorption performance, Ceram. Int. 44 (2018) 18886–18893, https://doi.org/10.1016/j.ceramint.2018.07.124.
[58] L. Wang, B. Shi, Hydroxide conduction enhancement of chitosan membranes by functionalized MXene, Mater. (Basel) 11 (2018), https://doi.org/10.3390/ma11112335.
[59] B.M. Jun, J. Heo, N. Taheri-Qazvini, C.M. Park, Y. Yoon, Adsorption of selected dyes on Ti3C2Tx MXene and Al-based metal-organic framework, Ceram. Int. 46 (2020) 2960–2968, https://doi.org/10.1016/J.CERAMINT.2019.09.293.
[60] X. Gao, Z.K. Li, J. Xue, Y. Qian, L.Z. Zhang, J. Caro, H. Wang, Titanium carbide Ti3C2Tx (MXene) enhanced PAN nanofiber membrane for air purification, J. Memb. Sci. 586 (2019) 162–169, https://doi.org/10.1016/j.memsci.2019.05.058.
[61] J. Chen, X. Yuan, F. Lyu, Q. Zhong, H. Hu, Q. Pan, Q. Zhang, Integrating MXene nanosheets with cobalt-tipped carbon nanotubes for an efficient oxygen reduction reaction, J. Mater. Chem. A. 7 (2019) 1281–1286, https://doi.org/10.1039/c8ta10574j.
[62] G.P. Lim, C.F. Soon, M. Morsin, M.K. Ahmad, N. Nayan, K.S. Tee, Synthesis, characterization and antifungal property of Ti3C2Tx MXene nanosheets, Ceram. Int. 46 (2020) 20306–20312, https://doi.org/10.1016/j.ceramint.2020.05.118.
[63] W. Feng, H. Luo, Y. Wang, S. Zeng, L. Deng, X. Zhou, H. Zhang, S. Peng, Ti3C2 MXene: A promising microwave absorbing material, RSC Adv. 8 (2018) 2398–2403, https://doi.org/10.1039/c7ra12616f.
[64] J. Zhu, Y. Tang, C. Yang, F. Wang, M. Cao, Composites of TiO 2 Nanoparticles Deposited on Ti 3C 2 MXene Nanosheets with Enhanced Electrochemical

Performance, J. Electrochem. Soc. 163 (2016) A785–A791, https://doi.org/10.1149/2.0981605jes.
[65] S. Alekseev, D. Korytko, M. Iazykov, S. Khainakov, V. Lysenko, Electrochemical synthesis of carbon fluorooxide nanoparticles from 3C-SiC substrates, J. Phys. Chem. C. 119 (2015) 20503–20514, https://doi.org/10.1021/acs.jpcc.5b06524.
[66] J. Guo, Y. Sun, B. Liu, Q. Zhang, Q. Peng, Two-dimensional scandium-based carbides (MXene): band gap modulation and optical properties, J. Alloy. Compd. 712 (2017) 752–759, https://doi.org/10.1016/j.jallcom.2017.04.149.
[67] Y. Zhang, W. Xia, Y. Wu, P. Zhang, Prediction of MXene based 2D tunable band gap semiconductors: GW quasiparticle calculations, Nanoscale 11 (2019) 3993–4000, https://doi.org/10.1039/c9nr01160a.
[68] J.B. Islam, M. Furukawa, I. Tateishi, H. Katsumata, S. Kaneco, Photocatalytic reduction of hexavalent chromium with nanosized TiO2 in presence of formic acid, Vol. 3, Page 33, ChemEngineering 2019 (3) (2019) 33, https://doi.org/10.3390/CHEMENGINEERING3020033.
[69] J. Zhang, W.N. Wang, M.L. Zhao, C.Y. Zhang, C.X. Huang, S. Cheng, H.M. Xu, H. S. Qian, Magnetically Recyclable Fe3O4@ZnxCd1-xS Core-Shell Microspheres for Visible Light-Mediated Photocatalysis, Langmuir 34 (2018) 9264–9271, https://doi.org/10.1021/ACS.LANGMUIR.8B01413/SUPPL_FILE/LA8B01413_SI_001.PDF.
[70] H. Zhao, Q. Xia, H. Xing, D. Chen, H. Wang, Construction of Pillared-Layer MOF as Efficient Visible-Light Photocatalysts for Aqueous Cr(VI) Reduction and Dye Degradation, ACS Sustain, Chem. Eng. 5 (2017) 4449–4456, https://doi.org/10.1021/ACSSUSCHEMENG.7B00641/SUPPL_FILE/SC7B00641_SI_002.CIF.
[71] F.X. Wang, X.H. Yi, C.C. Wang, J.G. Deng, Photocatalytic Cr(VI) reduction and organic-pollutant degradation in a stable 2D coordination polymer, Chin. J. Catal. 38 (2017) 2141–2149, https://doi.org/10.1016/S1872-2067(17)62947-4.
[72] U. Khalil, M.B. Shakoor, S. Ali, S.R. Ahmad, M. Rizwan, A.A. Alsahli, M. N. Alyemeni, Selective removal of hexavalent chromium from wastewater by rice husk: Kinetic, isotherm and spectroscopic investigation, Water (Switz.) 13 (2021) 263, https://doi.org/10.3390/w13030263.
[73] T.D. Ntuli, T.H. Mongwe, L.L. Sikeyi, O. Mkhari, N.J. Coville, E.N. Nxumalo, M. S. Maubane-Nkadimeng, Removal of hexavalent chromium via an adsorption coupled reduction mechanism using olive oil derived carbon nano-onions, Environ. Nanotechnol., Monit. Manag. 16 (2021), 100477, https://doi.org/10.1016/j.enmm.2021.100477.
[74] M. Shirzad-Siboni, M. Farrokhi, R. Darvishi Cheshmeh Soltani, A. Khataee, S. Tajassosi, Photocatalytic reduction of hexavalent chromium over ZnO nanorods immobilized on kaolin, Ind. Eng. Chem. Res. 53 (2014) 1079–1087, https://doi.org/10.1021/ie4032583.
[75] N.H. Alias, J. Jaafar, S. Samitsu, T. Matsuura, A.F. Ismail, S. Huda, N. Yusof, F. Aziz, Photocatalytic nanofiber-coated alumina hollow fiber membranes for highly efficient oilfield produced water treatment, Chem. Eng. J. 360 (2019) 1437–1446, https://doi.org/10.1016/j.cej.2018.10.217.
[76] D. Jiang, Y. Yang, C. Huang, M. Huang, J. Chen, T. Rao, X. Ran, Removal of the heavy metal ion nickel (II) via an adsorption method using flower globular magnesium hydroxide, J. Hazard. Mater. 373 (2019) 131–140, https://doi.org/10.1016/j.jhazmat.2019.01.096.
[77] N.H. Mthombeni, S. Mbakop, S.C. Ray, T. Leswifi, A. Ochieng, M.S. Onyango, Highly efficient removal of chromium (VI) through adsorption and reduction: A column dynamic study using magnetized natural zeolite-polypyrrole composite, J. Environ. Chem. Eng. 6 (2018) 4008–4017, https://doi.org/10.1016/j.jece.2018.05.038.
[78] A.L. Popovic, J.D. Rusmirovic, Z. Velickovic, T. Kovacevic, A. Jovanovic, I. Cvijetic, A.D. Marinkovic, Kinetics and column adsorption study of diclofenac and heavy-metal ions removal by amino-functionalized lignin microspheres, J. Ind. Eng. Chem. 93 (2021) 302–314, https://doi.org/10.1016/j.jiec.2020.10.006.
[79] Q.H. Li, M. Dong, R. Li, Y.Q. Cui, G.X. Xie, X.X. Wang, Y.Z. Long, Enhancement of Cr(VI) removal efficiency via adsorption/photocatalysis synergy using electrospun chitosan/g-C3N4/TiO2 nanofibers, Carbohydr. Polym. 253 (2021), 117200, https://doi.org/10.1016/j.carbpol.2020.117200.
[80] P.C. Okafor, C.O. Obadimu, Sol. Photo Degrad. Phenol. Using Cocos nucifera (Coconut) Shells adsorbent (2015), https://doi.org/10.15640/jcb.v3n1a3.
[81] N.K. Mondal, S. Chakraborty, Adsorption of Cr(VI) from aqueous solution on graphene oxide (GO) prepared from graphite: equilibrium, kinetic and thermodynamic studies, Appl. Water Sci. 10 (2020), https://doi.org/10.1007/S13201-020-1142-2.
[82] J. Bu, W. Li, N. Niu, N. Guo, H. Zhou, C. Chen, A. Ding, Adsorption of Cr(VI) from wastewater by iron-modified coconut shell biochar, E3S Web Conf. 248 (2021), https://doi.org/10.1051/E3SCONF/202124801059.
[83] S. Singh, A.G. Anil, S. Khasnabis, V. Kumar, B. Nath, V. Adiga, T.S.S. Kumar Naik, S. Subramanian, V. Kumar, J. Singh, P.C. Ramamurthy, Sustainable removal of Cr (VI) using graphene oxide-zinc oxide nanohybrid: Adsorption kinetics, isotherms and thermodynamics, Environ. Res. 203 (2022), 111891, https://doi.org/10.1016/J.ENVRES.2021.111891.
[84] M. Malakootian, F. Mansuri, Hexavalent chromium removal by titanium dioxide photocatalytic reduction and the effect of phenol and humic acid on its removal efficiency, Int. J. Environ. Health Eng. 4 (2015) 19, https://doi.org/10.4103/2277-9183.157720.
[85] S. Mor, K. Ravindra, N.R. Bishnoi, Adsorption of chromium from aqueous solution by activated alumina and activated charcoal, Bioresour. Technol. 98 (2007) 954–957, https://doi.org/10.1016/J.BIORTECH.2006.03.018.
[86] T.A. Khan, M. Nazir, I. Ali, A. Kumar, Removal of Chromium(VI) from aqueous solution using guar gum–nano zinc oxide biocomposite adsorbent, Arab. J. Chem. 10 (2017) S2388–S2398, https://doi.org/10.1016/J.ARABJC.2013.08.019.
[87] S.A. Chaudhry, T.A. Khan, I. Ali, Equilibrium, kinetic and thermodynamic studies of Cr(VI) adsorption from aqueous solution onto manganese oxide coated sand grain (MOCSG,), J. Mol. Liq. 236 (2017) 320–330, https://doi.org/10.1016/J.MOLLIQ.2017.04.029.
[88] T.A. Khan, V.V. Singh, Removal of cadmium(II), lead(II), and chromium(VI) ions from aqueous solution using clay, Toxicol. Environ. Chem. 92 (2010) 1435–1446, https://doi.org/10.1080/02772241003592930.
[89] I.-I.N. Etim, P.C. Okafor, R.A. Etiuma, C.O. Obadimu, Solar photocatalytic degradation of phenol using Cocos nucifera (coconut) shells as adsorbent, J. Chem. Biochem. 3 (2015) 35–45, https://doi.org/10.15640/jcb.v3n1a3.
[90] X. Wang, Y. Liang, W. An, J. Hu, Y. Zhu, W. Cui, Removal of chromium (VI) by a self-regenerating and metal free g-C3N4/graphene hydrogel system via the synergy of adsorption and photo-catalysis under visible light, Appl. Catal. B Environ. 219 (2017) 53–62, https://doi.org/10.1016/j.apcatb.2017.07.008.
[91] C.C. Yang, K.C. Dao, Y.S. Lin, T.Y. Cheng, K.F. Chen, Y.P. Tsai, Impacts of mixing mode on photocatalytic reduction of hexavalent chromium over titanium dioxide nanomaterial under various environmental conditions, Water (Switz.) 13 (2021) 1–16, https://doi.org/10.3390/w13162291.
[92] A. Jain, A. Kumar, H. Kaur, V. Krishnan, Strategic combination of ultra violet-visible-near infrared light active materials towards maximum utilization of full solar spectrum for photocatalytic chromium reduction, Chemosphere 267 (2021), 128884, https://doi.org/10.1016/J.CHEMOSPHERE.2020.128884.
[93] J. He, P. Wu, L. Chen, H. Li, M. Hua, L. Lu, Y. Wei, Y. Chao, S.S. Zhou, W. Zhu, H. Li, Dynamically-generated TiO2 active site on MXene Ti3C2: Boosting reactive desulfurization, Chem. Eng. J. 416 (2021), 129022, https://doi.org/10.1016/J.CEJ.2021.129022.
[94] Y. Chae, S.J. Kim, S.Y. Cho, J. Choi, K. Maleski, B.J. Lee, H.T. Jung, Y. Gogotsi, Y. Lee, C.W. Ahn, An investigation into the factors governing the oxidation of two-dimensional Ti3C2 MXene, Nanoscale 11 (2019) 8387–8393, https://doi.org/10.1039/C9NR00084D.
[95] X. Li, Y. Bai, X. Shi, N. Su, G. Nie, R. Zhang, H. Nie, L. Ye, Applications of MXene (Ti3C2Tx) in photocatalysis: a review, Mater. Adv. 2 (2021) 1570–1594, https://doi.org/10.1039/D0MA00938E.